5-21-2004

Investigation of Surface Displacements Induced in Loaded Cross-Ply Composite Laminates with Microcracking

Balakishore Rayasam
University of New Orleans

INVESTIGATION OF SURFACE DISPLACEMENTS INDUCED IN LOADED CROSS-PLY COMPOSITE LAMINATES WITH MICROCRACKING

A Thesis

Submitted to the Graduate Faculty of the
University of New Orleans
in partial fulfillment of the
requirements for the degree of

Masters of Science
in
The Department of Mechanical Engineering

by

Balakishore V Rayasam
B.Tech, Nagarjuna University, 2000
May 2004

Acknowledgements

I would like to thank Dr. Melody Verges for introducing me to the field of microcracking in composites and for all her continuous and patient support. This study was carried out with her vision and ideas.

I would also like to thank Dr. Paul Herrington for clarifying my doubts on ANSYS.

I wish to thank Dr. Paul J Schilling for attending the defense and his graduate students Arun Kumar and Bhanu for their guidance in documentation.

I wish to thank to Krishna Kumar Kasturi and Rajiv Mididoddi for their help on drawings.

Finally I would like to thank my parents and friends for all their support and motivation.

Table of Contents

List of Figures

LIST OF TABLES

Abstract

This work is aimed at investigating out-of-plane displacement data on the top surface of a loaded composite laminate containing microcracking damage to explore the feasibility of using surface data to locate microcracks in laminates. In this study, finite element models are created for eleven different cross-ply IM7/977-2 laminates with ply numbers varying from four to ten. Here, each ply thickness is 0.127mm, which is the common laminate thickness commercially available for this material system. For each model a range of transverse loadings are applied and the surface displacement data are analyzed along the mid-plane perpendicular to the plane of the crack. The following out-of-plane surface data parameters are obtained for each case: the minimal value above the crack tip, the peak value, and the far-field value. The difference in the peak and minimal values for a given loading is important in determining whether or not the optical technique is sensitive enough to resolve the data. The lateral distance to the peak values and the far-field values are also obtained. These distances are important in determining whether or not an optical system can spatially resolve the data. Results suggest that an optical technique such as digital holography could resolve, at a minimum, the data of [0/90/90/0], [0/90/90/90/90/0], and [0/0/90/90/90/90/0/0] laminates subjected to transverse loads of 1000 MPa.

Introduction

Material selection in any technical development is of utmost importance. An increase in demand for stiff and lightweight materials has caused industries such as the aerospace industry to focus on the feasibility of integrating composite materials into structures. As composites become more and more popular, the need for the investigation of failure phenomenon has also increased. It has been observed that the first form of damage in any composite laminate subjected to transverse loading is microcracking, which is an intralaminar or ply crack that traverses the thickness of the ply and runs parallel to the fibers in that ply. The immediate effect of this microcracking is degradation in thermo-mechanical properties of the laminate. The secondary effect of microcracking includes nucleation of other forms of damage. In industries such as the aerospace industry identification of these microcracks are crucial from a structural as well as a permeability standpoint.

The purpose of the present investigation is to investigate the plausibility of utilizing a new method for the identification of microcracking in composite materials. This method was first proposed by Larson et al. (1999) for the identification of flaws in homogeneous materials. In that work the investigators loaded cubes of acrylic material containing penny-shaped and elliptical-shaped flaws in Mode-I loading and gathered out-of-plane surface displacement data on a nearby surface. These displacements were gathered in real time as a function of loading by a technique called holographic

interferometry. These researchers noted that the out-of-plane contours on the surface changed depending on the shape, size and depth of the crack. Herrington et al. (2002) [ref 13] performed a finite element analysis on the same experimental specimen tested by Larson et al. (1999). They concluded that for a penny-shaped crack the displacement pattern on the surface was unique; i.e., only one crack radius and depth combination could yield a given surface contour pattern. These researchers further noted that crack parameters (radius and depth) could be derived solely by several surface displacement parameters. These parameters included (a) the minimum value of out-of-plane displacement (located in the plane of crack), (b) the peak value of displacement, and (c) the lateral distance of the peak value as shown in Figure 1.1.

In using such a method for the identification of microcracking several issues must be investigated. Composites are very stiff materials. It stands to reason that as the stiffness of a material increases, a larger load would be required to obtain any noticeable displacements of the surface. Furthermore, the shape and size of a microcrack is very different than the crack studied in the previous research. A microcrack is a through crack that is smaller in size in than the 1 inch radius penny-shaped crack studied previously. Therefore, it would stand to reason that the surface displacements will be harder to identify.

In this work a finite element analysis is used to study how the loading and ply lay-up will effect the out-of-plane surface displacement pattern. In addition, several optical techniques will be investigated. Finally, a discussion will be provided on the plausibility of using such an approach for the identification of microcracking in composite materials.

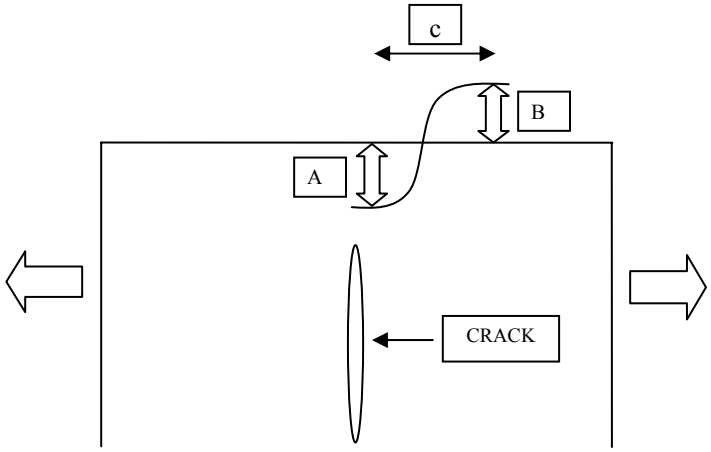

Figure 1.1 Schematic showing the surface displacement parameters used for characterizing penny-shaped cracks in homogeneous materials

This analysis is limited to cross-ply composites. The microcrack is considered in the 90° fibers only and is assumed to extend along the entire width of the composite laminate. Simulations are carried out by changing the length of the crack (i.e., the thickness of the inner 90° ply group) and the thickness of the outer ply group. The resulting out-of-plane surface displacements are plotted against the length of laminate.

The following chapter discusses composite materials and types as well as failures in composite materials, concentrating mainly on failures under transverse loading (microcracking), several NDT techniques that are used to measure flaws in composites, and present techniques used to detect microcracking. Chapter 3 focuses on the NDT approach considered in this research. Chapter 4 provides a description of the finite element model and analysis created to test the feasibility of utilizing such an approach. Chapter 5 focuses on presenting the resulting surface displacement patterns for different lay-ups under investigation. Conclusions and recommendations for future work are discussed in chapter 6.

2. Literature Review

This chapter begins with a brief discussion of composites and types of composite failures, concentrating on the onset and progression of microcracking. A number of non-destructive testing techniques are also discussed in this chapter. Finally, techniques that have been used to identify microcracking are discussed.

2.1 Composites

A composite material is a macroscopic combination of two or more physically and/or chemically distinct, suitably arranged or distributed phases with an interface separating them. Composites are not only used for improving structural properties, but also for electrical, thermal, environmental properties. They have characteristics that are not depicted by any of the components in isolation. Modern composite materials are usually optimized to achieve a particular balance of properties for a given range of applications. The resulting composite material exhibits improved properties. The improved structural properties generally result from the load sharing mechanism. Typically, reinforcements are stronger and stiffer materials and the matrix acts to hold the fibers together. There are certain exceptions like rubber modified polymers, where reinforcements are more compliant and more ductile than the polymer, resulting in improved toughness.

According to Miracle and Donaldson (ref 6) composites can be classified at two levels. The first one is based on matrix constituent. The major classes in this classification are organic-matrix composites (OMC), metal-matrix composites (MMC) and ceramic-matrix composites (CMC). Organic-matrix composites include polymer matrix composites (PMC) and carbon-matrix composites. Carbon matrix composites are also known as carbon-carbon composites. A second type of classification is based on the reinforcement form. Particulate reinforcements, whisker reinforcements, continuous fiber laminated composites and woven composites are grouped into this type of classification. Generally the volume fraction of reinforcements will be at least 10%. Reinforcement is considered to be a particle if all dimensions of the reinforcement are equal. Reinforcements shaped like spheres, flakes and rods of roughly equal axes are grouped in the particle classification. Whisker reinforcements will have an aspect ratio ranging from 20 to 100. Both of these reinforcements are called as discontinuous reinforcements because the reinforcements are discontinuous. Other than these reinforcements, sometimes there are also materials, usually polymers. These are generally referred as filled systems, because filler particles are included for the purpose of cost reduction. Continuous fiber reinforced composites will have reinforcement lengths much greater than their cross sectional dimensions. Most of the fibers in continuous fiber reinforced composites have lengths that are comparable to the overall dimensions of the composite. Because of small cross-sectional area, fibers cannot be used in structures directly. Hence they are embedded in matrix to form fiber-reinforced composites. Matrix binds the fibers and transfers the load.

From Agarwal and Broutman, (1990) [ref 7], fiber-reinforced composites can be classified as single-layered and multi-layered composites. Single-layered composites have several distinct layers with each layer having the same orientation and properties. Most composites used in structural applications are multi-layered. With multi-layered composites, each layer can be oriented differently. The directional material properties change based on the orientation of the layers (plies). Each ply typically has a thickness varying from 0.1-0.2 mm. When the constituent materials in each layer are the same, though the orientation of fibers is different, they are known as laminates. These laminates will give improved wear, impact and thermal resistances. Properties and orientations of the laminae are chosen based on design requirements. Fiber composites are heterogeneous materials. They fall under the orthotropic material class, whose behavior lies in between isotropic and anisotropic materials. In general, the deformation behavior of an orthotropic material is similar to anisotropic material. However, when loads are applied in axes of symmetry direction, they behave like isotropic materials.

The final category of composites is formed by weaving, braiding or knitting the fiber bundles to create interlocking fibers. These fibers will have an orientation that is orthogonal to primary structural plane. These composites will have improved properties in the out-of-plane direction.

2.2 Failure in Composites

Failure in fiber-reinforced composites is generally produced by the accumulation of several types of internal damage. Damage includes fiber breaking, microcracking, delamination, interface debonding, etc.. The type of failure will depend

on loading and material properties (fiber, matrix and interface). The damage will be distributed through out the composite and increases with the loading. This damage that is distributed through out the composite will unite to form a macroscopic fracture before failure.

Under longitudinal tensile loading failure initiates by fiber breakage at the weakest cross-section. As the number of broken fibers increases, some cross-section of composite will become too weak causing complete rupture of the composite. This is called brittle failure. If the interfaces of broken fibers are debonded because of stress concentrations created at the fiber ends and thus leading separation of composite at a given cross-section then that type of failure is called brittle failure with fiber pullout.

Under longitudinal compressive loading fibers act as long columns and micro buckling may be possible. If fibers are buckled independent of each other then that mode of buckling is called buckling in extension mode. If they are buckled relative to each other then that buckling is called buckling in shear mode. Buckling mainly depends on inter fiber distance

According to J.A.Nairn [ref 8], the first form of damage in composite laminates with the fibers subjected to a transverse loading is matrix microcracking. These cracks run through the thickness of ply, parallel to fibers in that ply. These cracks are also known as matrix microcracks, ply cracks, microcracks, transverse cracks etc. They tend to develop under tensile, fatigue and thermal loadings. Microcracks usually form in the plies which are off-axis to the loading direction. These cracks will degrade the thermo-mechanical properties of the laminate. Upon an increase in loading, these cracks can nucleate other forms of damage like delamination. In an environment such as water or

moist air, the micro-cracked laminate will absorb considerably more water than uncracked laminate. This will then lead to an increase in weight, moisture attack on the resin and fiber-sizing agents, loss of stiffness, and, with time, an eventual drop in ultimate properties. In addition, these cracks could possibly link up together or with other types of damage to produce pathways for leakage.

The formation of the first crack is called the initiation or the onset of microcracking. Garrett and Bailey (1997), [ref 21] conducted many experiments on microcracking in $[0/90]_s$ laminates made of glass-reinforced epoxy laminates. They varied the thickness of 90° ply keeping thickness of 0° ply constant. They observed that the thickness of 90° ply has a significant effect on microcrack initiation. They found that as the thickness of the 90° ply is decreased in proportion to the thickness of 0° ply, the strain to microcrack initiation increases. They observed that when the 90° ply thickness is still decreased than 0° ply thickness microcracks are suppressed entirely and the laminate fails before the initiation of any microcracking. Flaggs and Kural (1982), [ref 20] conducted experiments on microcracking in carbon fiber/epoxy laminates. They also observed that strain to initiate microcracking increases as the thickness of 90° plies decreases in proportion to the thickness of the 0° plies.

The schematic in figure 2.1 illustrates the progression of microcracking in the 90° plies of a composite laminate. In general, it is assumed when two microcracks are present that the next microcrack will form halfway between the two that are present. As shown in schematic 2.1 (b) and (c) a microcrack forms instantaneously at a given load. Also, as shown in the schematic, it extends through the thickness of the 90° ply group.

Although the width of the laminate is not shown in this schematic, the microcrack generally extends through the width as well. Therefore, the microcrack is often thought of as a rectangular crack possessing the same thickness and width dimensions as that of the 90° ply group.

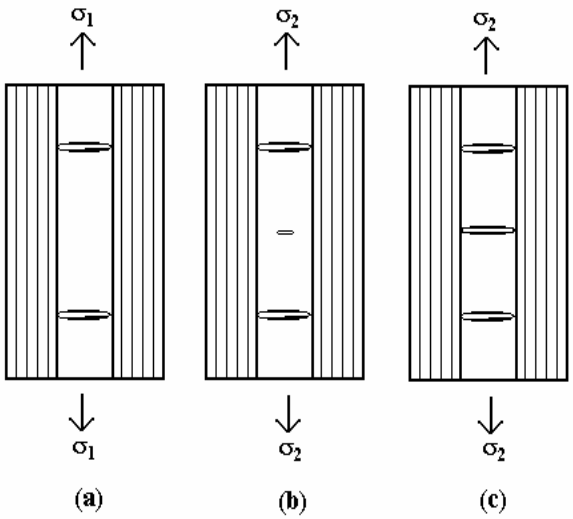

Figure 2.1. Schematic of microcrack development and progression in 90° ply upon application of transverse loading. (a) Microcrack development at an applied load σ_1. (b) Initiation of a microcrack at an applied load σ_2 ($\sigma_2>\sigma_1$). (c) Progression of microcrack at same applied load σ_2.

2.3 Non-Destructive Testing

According to Bray and Stanley (1997) [ref 9], NDT techniques are characterized as active and passive, or surface and volumetric. In active techniques some form of energy will be introduced into the specimen and the output energy is measured. If there are any flaws then a notable change in the input energy can be expected. Eddy current, magnetic, ultrasonics, radiography etc will fall into this category. In passive techniques some kind of reaction is expected from the specimen and by measuring that reaction flaws can be estimated. Acoustic emissions, visual inspection, leak reaction, and

penetrant techniques are of this type. Surface techniques are the techniques in which flaws nearer to the surface are measured and certain modifications for these techniques will help in measuring flaws away from the surface. Electro magnetic methods are usually limited to finding flaws nearer to the surface. Volumetric methods like ultrasonics, acoustic emissions are useful in measuring the flaws away from the surface.

Factors considered when choosing an appropriate technique are size and orientation of the flaw, type of material, etc. In general, the detection of small flaws will need more sophisticated techniques when compared to large flaws. In most cases, prior defect history of the part will help in selecting the proper NDT technique. Understanding the operation of each and every technique is necessary before selecting the technique. Existing NDT methods currently useful for crack detection include acoustic emission, radiography, ultrasonic inspection, and eddy current inspection.

2.3.1 Visual inspection

With visual inspection, identification of flaws is done visually or by measuring the dimensions of the specimen. It is useful only for large flaws and chances of missing smaller flaws are very high. Therefore, this method can be useful at a macroscopic level not but not microscopically.

2.3.2 Penetrant Inspection

Penetrant inspection is based on the principle of capillarity. In this method penetrant is accumulated around a discontinuity to create a recognizable indication of the crack or any other surface opening. Capillary action attracts the penetrant into the void in a greater concentration than its heavier surroundings. Sufficient care should be taken for surroundings contrast to identify the penetrant describing flaw

size and shape. This method is not suitable for nonporous and nonmagnetic materials. This method can be used for identifying the subsurface flaws or crack openings. A crack or opening that did not reach the surface would not be identified. Thorough consideration of the surface and fluid properties and the flaw recognition system are the keys for success of this technique.

2.3.3 Acoustic emission testing

Acoustic emission testing is a passive technique, which uses elastic techniques generated by cracks, fiber breaks for identifying the defects. In metals and concrete these acoustic waves are generated by local stress redistributions associated with motion of dislocations and cracks. In composites these waves are generated by variety of actions like cracking, separation of fibers and the matrix. Acoustic emission monitoring systems simply listen to sounds generated by the material. The emission signal is strain related. Material conditions effect the transmission of emission signals. For example, in metals it depends on grain size and in composites distribution of the matrix and fiber.

Acceptance of this method is justified on economic basis due to the reduced labor. The disadvantage with this technique is that the size of the defects can not be determined. It is often necessary that these emission sources be inspected by some other NDT techniques like ultrasonics or radiography for assessing the size.

2.3.4 Ultrasonic Inspection

This technique is based on the principles of reflection and refraction. With this technique, sound waves of short wavelength and high frequency are used to detect flaws or measure surface displacements. Ultrasonic waves (frequency should be at least 20kHz) are passed through the specimen and the frequency and time of the reflected

waves are measured. These waves are often considered in the form of pulses of energy rather than continuously excited waves. A transducer, which emits ultrasonic pulses, is placed on the specimen. Typically transducers are made of piezoelectric materials. These materials have the behavior of converting mechanical vibrations to electric pulses and vice versa. The pulses that travel through the object are reflected and refracted by defects in the object. These pulses are then detected by a receiver, which determines the existence of defect by loss in signal amplitude.

This method can be applied to any material provided that the material transmits mechanical vibrations. This method is useful in detecting deep surface flaws and it also gives the details about the depth of crack. Disadvantages of this technique are that the test object should be a good conductor of sound, it is not suitable for complex-shaped materials, and it also needs the transducer to be in contact with object.

2.3.5 Radiography

The basic principle of radiography involves propagating energy from a source through a test object, and evaluating the energy pattern received on the opposite side. The emitted radiation energy from the source is made to pass through the object. The evaluation of the condition of the object is done using the pattern of a series of gray shades between black and white. A recording plane opposite to the source is used to record the image. This image is a result of difference in attenuation rates, or absorption, for various types of matter. An image of a defect will occur on the recoding plane (film), provided that there is a sufficient difference in the radiation intensities received by the film under the defect as compared to that received through the remainder of the material. Generally where the defect is a void or porosity, image will be darker than the

surroundings. Gamma ray and X ray sources are the typically used radiation energy sources. The energy level of source can be determined by voltage. High voltage will result in short wavelength and the amount of current will determine the number of rays produced.

Radiography is most satisfactory for finding internal, nonplanar defects such as voids and porosity. Planar defects can also be detected with proper orientation. It is also useful in detecting changes in material composition. Depth of an object or void cannot be measured from a single radiographic inspection. The disadvantage of this technique is that X-rays and gamma rays are hazardous.

2.3.6 Tomography

Tomography is used to reconstruct the interior structural details. Characteristics such as shape, displacements, internal flaws, and density are measured by this technique. High quality and very clear cross sectional images can be produced with this technique. According to Schilling et. al. [ref 12], in this technique an image of the specimen is recorded to analyze the internal structure. A number of two-dimensional images are gathered by rotating either the source and detector assembly or by rotating the specimen, in order to construct a 3-D image. Tomography has a wide range of applications in medical and ceramic fields.

The main parts in a tomography set-up are a source, a collimator, and a receiver. The test specimen is placed between the source and the receiver (imaging system). X-rays are allowed to transmit through the specimen and the receiver measures the total radiation reached through the object. Images are created, due to the difference in absorption rate between the specimen and the medium in which specimen is kept. This

will be stored in the memory. After the initial scan the source-detector assembly (or the specimen holder) will be rotated through a very small step of angle and the procedure continues for a number of such rotation angles through a total of 180° as it covers the entire object. This process is called data acquisition. After acquiring data image reconstruction will be done. If an unknown object is present inside the specimen a change in absorption can be noticed in the image. This image is stored in the memory. Reconstruction mainly contains estimation of attenuation for each image from projection data. As the object is rotated through a small angle, a new image is formed. All these images are combined to localize the position of absorption point inside the area of reconstruction. This process is called “back-projection”. With increase in number of shadow projections, position and shape of absorption can be estimated accurately. Hence in ideal case, infinite number of projections should result in exact shape. But at the same time a blur image around the point of absorption is formed because of superposition of lines will be formed. The process of elimination of the blur area in the back projection process is known as convolution. All cross-sectional shadows formed along the length of specimen are combined to get the exact shape and size of the specimen.

As mentioned earlier computed tomography is a specialized technique of radiography. If X-ray computed tomography results in very high resolution then it can be called microtomography. With microtomography a spatial resolution of few microns can be obtained. The main limitation of this process is the small size of the specimen and the need for it to be enclosed in the tomography machine.

2.3.7 Eddy current inspection

In this technique eddy currents are induced in the test object by changing the magnetic field near to it. Changing the current in a conductor creates this magnetic field. Eddy currents created in test object will generate another magnetic field, which will oppose the original one. These fields are detected by electro magnetic induction in a coil or by sensors. In many cases same coils are used to create these eddy currents and also to detect these fields. The presence of a flaw increases the resistance to the flow of eddy currents. This change is electronically analyzed to provide the information about type of flaw, flaw severity or material condition information. This technique can be used for conductive materials only. This is not useful in giving the exact size and shape of the defect.

2.4 Identification of Microcracking

The most popular and conventional method for gathering microcracking information about a specimen involves cutting through the thickness of the composite and using an optical microscope to view the microcracks. A few NDT techniques have also been reported in the literature that identify microcracking. These include radiography, ultrasonics, and microtomography.

Vikram and Lagoudas [ref 11] conducted experiments on cracked specimens using a polar back scattering technique. Fig 2.3 and 2.4 illustrates the general configuration of polar back scattering technique. A transducer is used to generate ultrasonics. The ultrasound is reflected by the crack and ply boundaries back to receiver. In this case the transducer itself is the receiver. The incident ray is reflected back towards the transducer only when the projection of incident ray onto the laminate is perpendicular

to the crack faces. Fig 2.4 better depicts this phenomenon. The transducer receives the backscattered signal only when the plane containing crack and the plane containing the transducer axis are perpendicular to each other.

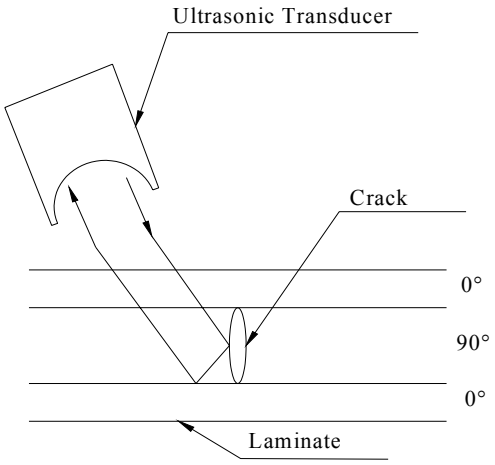

Fig 2.3 Schematic of ultrasonic polar backscattering technique.

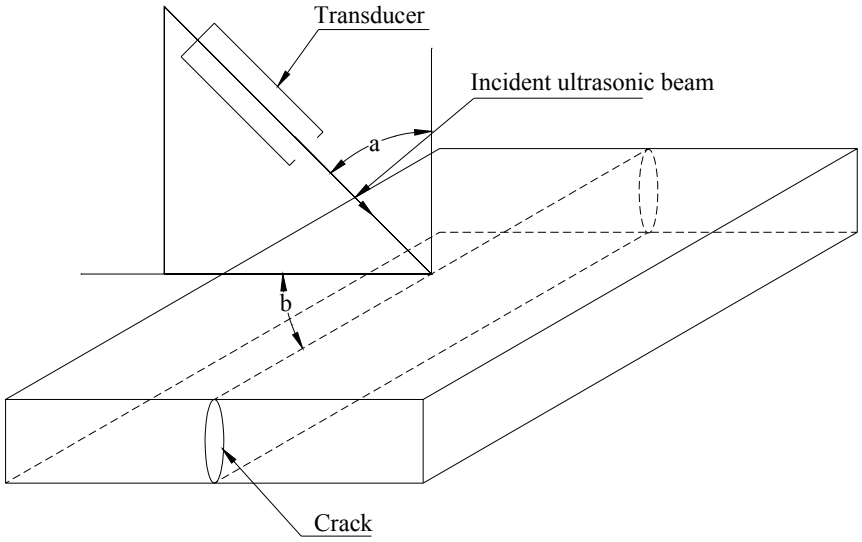

2.4 Schematic showing the planes of the transducer and the crack.

Several researchers have identified microcracks in laminates using radiography. However, because radiographs yield a two-dimensional image, deciphering the microcracking data contained in each ply is not feasible. Larson et al. (1999) [ref 1] used microtomography to detect microcracking in $[0/90]_s$ laminates. In that work, the microcracks were characterized in three-dimensions.

3 NDT Approach

As mentioned in the introduction, the long-term goal is to develop another NDT technique that would be useful in characterizing microcracking in composite laminates. Again, this technique was originally proposed by Larson et al. (1999) [ref 1] for use on homogeneous materials and is a coupled experimental and computational technique. An optical technique is used to gather surface data, while a computational technique is responsible for assessing the internal flaws based on the surface data. The next section is dedicated to proposing an experimental method that may be used to induce surface deformations in cracked specimens while the final section discusses some possible optical techniques that may be used to gather these displacements.

Prior to conducting experiments, a finite element analysis of the procedure could deem useful in determining if the surface displacement data is on the same order of magnitude as those that can be resolved by present optical techniques. This issue is the focus of this report. Chapter 4 is dedicated to the development of such a model and chapter 5 is dedicated to presenting the magnitudes of the surface displacements for a number of cross-ply laminates subjected to load limits of 1000MPa and discussing the plausibility of this proposed experiment.

3.1 Proposed Experiment

The following steps outline the experimental procedure, which will be followed in order to test the feasibility of utilizing surface displacement data to

characterize microcracking in composite laminates. The first step involves gathering specimens with known microcracks in them. Verges et al. (2003) [ref 4], uniaxially tested a number of IM7/977-2 $[0/90]_s$ laminates at specified loads in a tensile substage to obtain crack density versus load data. The substage used in that work is pictured in Figure 3.1. Each of these specimens was then inspected via microtomography for microcracking. Some of these specimens having only a couple of microcracks in them will be used in the initial tests. IM7/977-2 $[0/90/90]_s$ and $[0/0/90/90]_s$ specimens will also be loaded and examined for microcracks via microtomography.

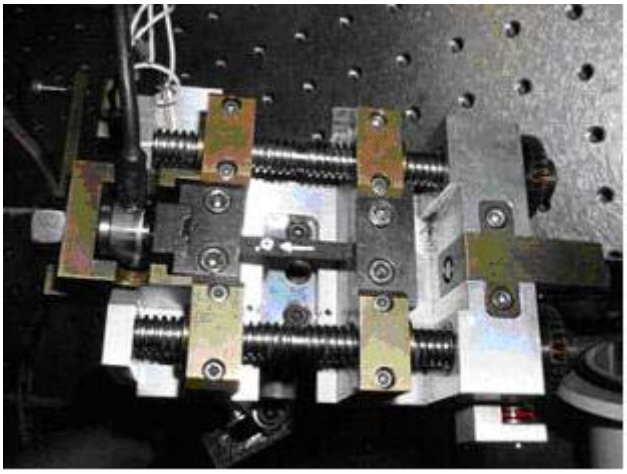

Figure 3.1 Tensile substage used to load the specimen

The second step involves loading these cracked specimens in the tensile substage. In the work done by Larson et al. (1999) [ref 1], microcracks did not initiate in the specimens until a load of 1100 MPa was reached. In order to insure no additional microcracking, the maximum loading on the [0/90/90/0] specimens will be limited to 1000 MPa.

The third step involves utilizing an optical technique to measure the resulting surface deformation. As mentioned in the introduction, composites are very stiff materials and quite large loads are needed to induce any recognizable surface deformation. The following section in this chapter discusses possible optical techniques that may be used in gathering this information. Keep in mind that all of these techniques can be used in real time; i.e., the surface of the composite laminate will be examined as it is being loaded.

3.2 Optical techniques

Optical techniques have high sensitivity and full field analysis of inspected area. As with other NDT techniques, the components are inspected with out any physical contact. Unlike other NDT techniques, the information used in the analysis of the object under investigation is gathered from the surface. Therefore, only access to a surface of the specimen is required.

The main features of optical NDT techniques are non-contact, full-field, no initial preparation of the object (except in some cases where coating to the object is helpful) and no real time consumption of films etc. The main optical NDT methods include the moiré method, holographic interferometry, shearography and photogrametery [ref 15]. With the exception of the moiré technique, which is limited to obtaining in-plane surface displacement data, all of these techniques can be used to obtain out-of-plane surface data. Holographic interferometry, shearography, and photogrammetry will therefore be discussed a bit further in terms of basic principles, types of measurements, and sensitivity.

3.2.1 Holographic Interferometry

Holography is the method of storing and regenerating all the amplitude and phase information contained in the light that is scattered from an illuminated body. Because all the information is reproduced, the regenerated object beam is, in the ideal case, indistinguishable from the original. Since it is possible to record the exact shape and position of a body in two different states, movement or deformation can be measured.

When two beams of coherent light are made to intersect, the interference between the two beams causes the creation of a three dimensional pattern of interference fringes. The object beam and reference beam (a plane beam) are the two beams used for interference. As the plane wave and the object beam merge, they interact to create an interference pattern. Fringe pattern may be obtained at any particular cross-section by inserting a photographic emulsion on a plate or film. The optical system should remain stable enough so that the film is exposed to a stationary pattern. These interference fringes have a spatial frequency ranging from 2000-3000 lines/mm. The interference pattern on the film record can only be examined under high magnification. The photographic record of the wave interference pattern produced by two beams is called a hologram because it contains all data about the object and reference beams.

The basic idea of holographic interferometry is that the image formed in holography can be compared with another holographic image of that object. Holographic interferometry mainly contains two types of recording. First type is “frozen fringe” or double exposure. In this type of recording, recording medium contains the initial image and the image after the object is disturbed. Hence after the images are reconstructed, a

fringe pattern in the form of zebra markings is observed. The other type of recording is "real time" or "live fringe" recording. In this type of recording, recording medium is inserted back after the processing of the initial image. These markings will give the measure of dimensional changes in the object. If the object is disturbed by stress or moved a small amount then a pattern of interference fringes are formed. By counting those fringes and comparing with the initial image, the amount of displacement can be estimated. In traditional holography, the sensitivity of the system is on order of wavelength of the light and is usually a few tenths of a micrometer. In digital holography, the sensitivity is reported to be on the order of 10 nm [ref 15].

3.2.2 Shearography

Digital Shearography is an optical interferometric technique that measures surface strains caused by thermal or mechanical loading. Shearography inspects a full area simultaneously which is illuminated with a divergent laser beam. It is an optical method, which measures the derivatives of out-of-plane surface displacements. Hence it is easier to correlate defects with strain anomalies using shearography than displacement anomalies applying holography.

A digital shearography set-up is shown in figure 3.2. Just like with holography, there are two main steps in obtaining any shearographic measurement. The first step involves grabbing an the image before the object is loaded and the next one involves grabbing the image after the object is disturbed.

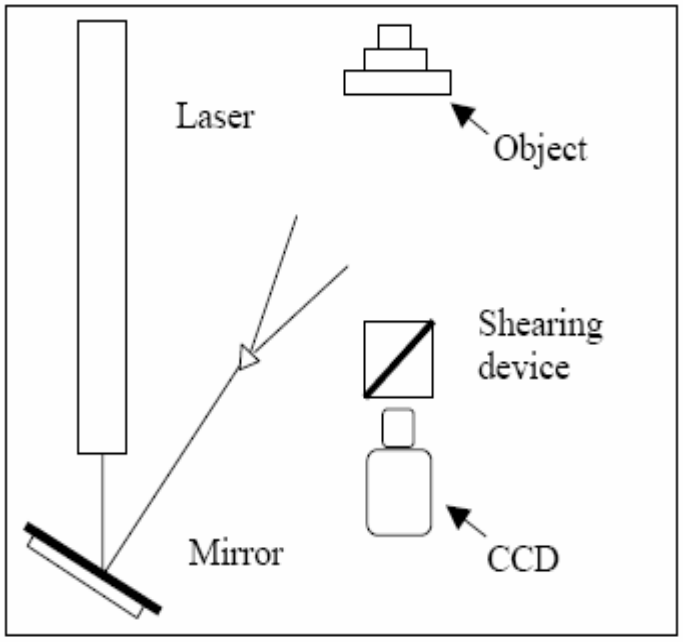

Figure 3.2 Schematic of a shearography set-up.

The object is illuminated with a coherent laser light inclined at a small angle to the surface and viewed through an image shearing device like Michelson interferomer. The effect of shearing is to map a point on the object into two points in the image. Introducing a glass wedge in front of the camera will shift the rays emanating from a point on the object away from the normal focal point of the lens as shown in figure 3.3.

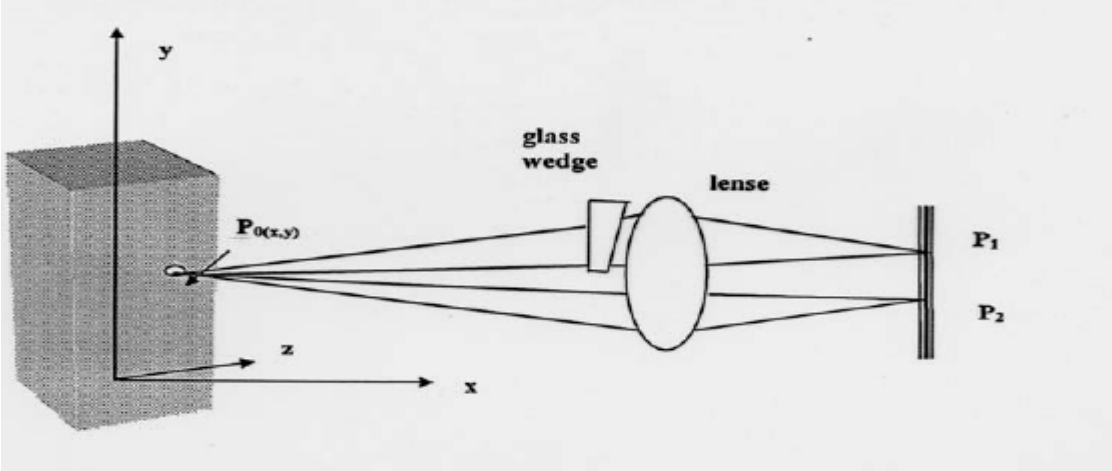

Figure 3.3 Schematic showing creation of lateral sheared images.

As the result of shearing action, the light reflected from the object is sheared or split, causing two separate images with slightly different path lengths from adjacent areas to be focused on the CCD as shown in figure 3.4. Reflected light from small adjacent portions of the total surface area is focused on each individual pixel. As illumination intensity of the light is constant, the intensity of light on each pixel will depend on the surface and shape of the object. Since each pixel gathers light from only a small portion of the field of view, the interference pattern is captured and recorded pixel by pixel in the computer, covering the entire field of view.

As the load is applied on the test object, it will cause change in the shape of the object and change the path length from point on the surface to each pixel on camera. The change in path length will cause a new intensity at each pixel, generating a new pattern. This pattern is also recorded [ref 17].

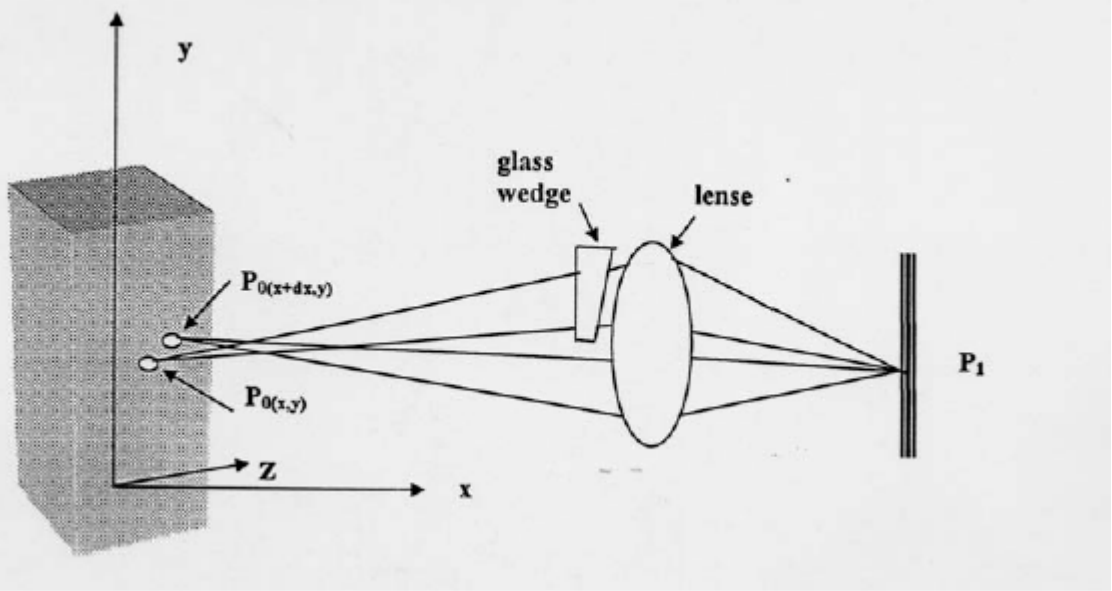

Figure 3.4 Schematic showing images being recombined.

Comparison of the two images gives the relative deformation at each point on the object. Sensitivity of this technique is almost in the same order as of holographic interferometry. A constant change in surface geometry represents no local deformation. The direction of shearing can be controlled by rotating the wedge in front of the camera lens or by tilting the mirror. This technique can be used successfully for complex shapes. But interpretation of results is not easy and the component must be loaded to see any kind of result. Only the gradient of deformation is measured.

3.2.3 Photogrammetry

The basic principle used in photogrammetry is triangulation. Photographs are taken from at least two locations. The line joining the camera position and object point is called line of sight. These lines of sight are intersected mathematically to get coordinates of the object. The main steps in this technique are photography and

metrology. Photography deals with the principles of photogrammetry and metrology is used for producing 3-dimensional coordinates from two-dimensional photographs.

Photography converts the real 3-dimensional objects into two-dimensional pictures. Hence some information about the object is lost, usually the third-dimension information. Photogrammetry maps the two-dimensional images back into 3-dimensional pictures. For this construction at least two pictures are needed. As the number of pictures used is increased, the dimensions of the object can be measured more accurately [ref 18].

The object under load is viewed by one or more cameras. A random or regular pattern with good contrast is applied to the surface of the test object, which deforms along with the object. The deformation under the load is recorded by CCD cameras and evaluated. Using photogrammetrical principles the 3D coordinates of the entire surface of the specimen are calculated. The 3D shape and deformations can be measured simultaneously. As long as the object remains with in the field of view of the cameras, all of the local deformations can be tracked. Sensitivity of this technique depends on field of view. For a 10 x 8 mm field of view sensitivity of this technique is around 0.3 microns, i.e. 300 nm [ref 19]. Note that the field of view can be altered depending on the magnification of the lens.

4 Finite Element Analysis

The finite element analysis of the model used in this study is a static, linear elastic analysis. ANSYS 8.0® finite element software is used for the finite element work performed and presented here. Appendix A contains the Ansys code used to perform the finite element analysis on a [0/90/90/0] laminate.

4.1 Model Geometry

The composite laminate modeled in this analysis is similar in geometry to the composite laminates tested by Larson et al. (1999) [ref 1]. As shown in figure 4.1, the reference laminate consists of $[0/90]_s$ plies. As with the laminates tested by Verges et al., the width of laminate is considered to be 5 millimeters. In accordance with the thickness of the plies tested, the baseline thickness of each ply in the model is taken to be 0.127 mm. Finally, the length of the laminate is taken to be 25.4 mm.

Because the loading on the laminate is symmetric about the plane of the microcrack, the actual finite element geometry is a quarter model of the laminate. As depicted in Figure 4.2, the quarter model is created such that the center of the microcrack is located at the left bottom-most point of the model. The corresponding dimensions are shown in figure 4.2. Global X, Y and Z axes are taken along the model length, height (thickness of the plies) and width. S.I. units are used in the analysis.

The quarter model depicted in Figure 4.2 consists of two layers. Each layer represents a ply of 0.127 mm thickness. The upper layer consists of fibers in 0º direction (parallel to the load) and the lower layer has fibers in the 90º direction. This

particular geometry is representative of the reference case. Other cross-ply geometries were also tested. In each

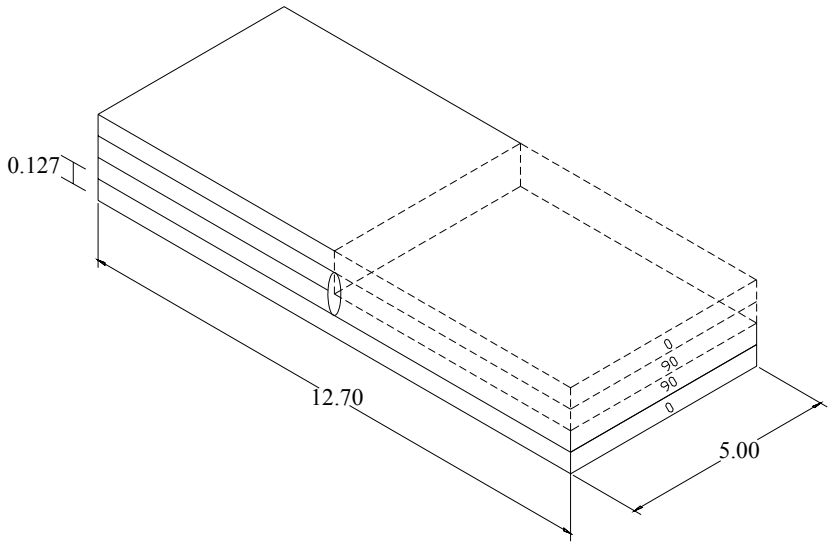

Fig 4.1 Schematic of $[0/90]_s$ composite laminate with microcrack in 90° plies.

case the microcrack is assumed to exist in the center of the laminate thickness. The thickness of each ply is 0.127 mm. Finally, it is assumed that for cases in which the 90º plies are adjacent to each other, the microcrack extends through the entire ply group.

4.2 Material Properties

In the work performed by Larson et al. (1999) [ref 1], three different types of fiber/resin systems were used. One of the material systems tested consisted of IM7 fibers with a 977-2 resin. The material properties used in this work are reflective of an IM7/977-2 material system. In the designed quarter model, PLY1 is considered to be the composite ply in which the fibers are oriented 90º to the applied load. As such, the ply is the stiffest in the *z*-direction (across the width of the laminate). Hence the material properties for PLY 1 are taken as follows: Young's moduli in the *x*, *y* and *z* directions are

$9.43x10^3$ N/mm^2, $9.43x10^3$ N/mm^2 and $159x10^3$ N/mm^2, respectively; the Poisson's ratios in the *xy*, *yz* and *xz* planes are 0.456, 0.253 and 0.253, respectively; and the shear moduli in the *xy*, *yz* and *xz* planes are $2.57x10^3$ N/mm^2, $4.34x10^3$ N/mm^2 and $4.34x10^3$ N/mm^2, respectively. PLY 2 is considered to be the composite ply in which the fibers are oriented parallel to the applied load. As such, the ply is the stiffest in the *x*-direction. According to choi and Sankar (2003) [ref 2], Young's moduli in the *x*, *y* and *z* directions are 15 $x10^3$ N/mm^2, $9.43x10^3$ N/mm^2 and $9.43x10^3$ N/mm^2, respectively. Poisson's ratios in the *xy*, *yz* and *xz* planes are 0.253, 0.456 and 0.253, respectively. Shear moduli in the *xy*, *yz* and *xz* planes are $4.34x10^3$ N/mm^2, $2.57x10^3$ N/mm^2 and $4.34x10^3$ N/mm^2, respectively [ref 2].

4.3 Meshing

Solid 45 elements possess the ability to include complex curve shapes without loosing accuracy. This element type is often preferred compared to other solid elements in ANSYS [ref 5]. Solid 45 is used for the three-dimensional modeling of solid structures. Eight nodes having three degrees of freedom at each node define the element. These solid 45 elements are used to generate the mesh for the entire model with the exclusion of the vicinity around the crack tip. Solid 95 elements are used around the crack tip. Figure 4.2 and 4.3 shows the schematic for solid 45 and 95 elements.

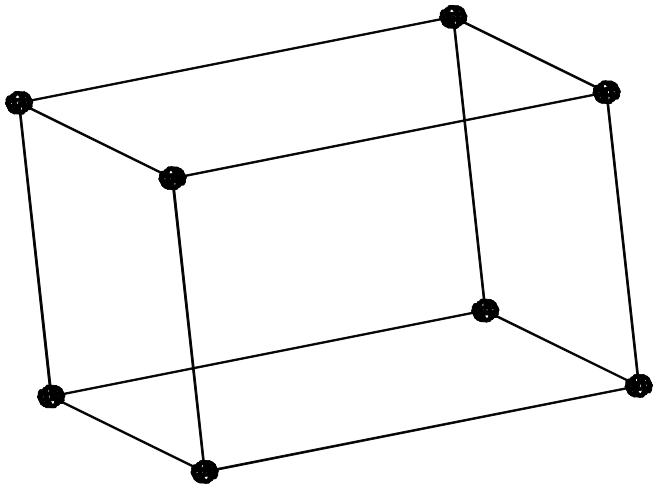

Figure 4.2 Schematic of a 8-noded solid 45 brick element.

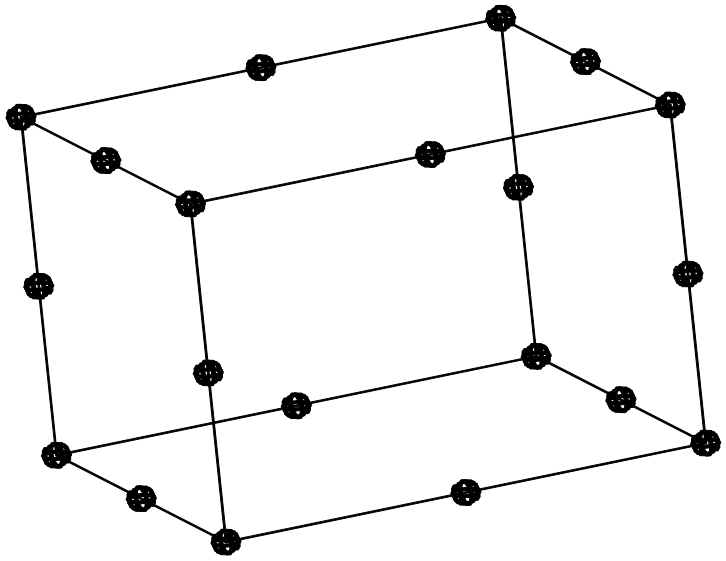

Figure 4.3 Schematic of a 20-noded solid 95 brick element.

Singular elements are always preferred around the vicinity of the crack tip. At the crack tip, four sided elements (in 2-D problems) are often degenerated down to triangles; for 3-dimensional problems, brick elements are degenerated into wedges. In elastic problems, the nodes at the crack tip are tied and the mid-side nodes are moved to quarter points. Such modifications result in a $1/\sqrt{r}$ strain singularity in the element, which

enhances numerical accuracy. A similar result can be achieved by moving mid-side nodes to quarter points in a four-sided element. But the singularity would only exist on the element edges; triangular elements are preferred in this case because the singularity exists with in the element as well as edges. The element is degenerated to a triangular one as in the case of elastic problems, but the crack tip nodes are united and the location of mid side nodes are unchanged. This element geometry produces 1/r strain singularity, which corresponds to the actual crack tip strain field for fully plastic, non-hardening materials.

For crack tip problems, the most efficient mesh design has proven to be the "spider web" configuration, which consists of concentric rings of four-sided elements that are focused towards the crack tip. The innermost ring of elements is degenerated to triangles. Since the crack tip region contains steep stress, strain gradients with the mesh refinement should be greatest at the crack tip. As per T.L.Anderson (2002) [ref 3], the spider web facilitates a smooth transition from a fine mesh at the crack tip to coarser mesh remote to the tip. Nodes are generated at their respective places and then elements are generated from nodes. Therefore, in this analysis, the mid-points are generated for the solid 45 elements, around the crack tip and then moved to the quarter distance. This is achieved by using a macro in the ANSYS program. The mesh at the crack tip for the quarter model is as shown in figure 4.4. An isotropic view of the entire mesh used in the quarter model is depicted in figure 4.5.

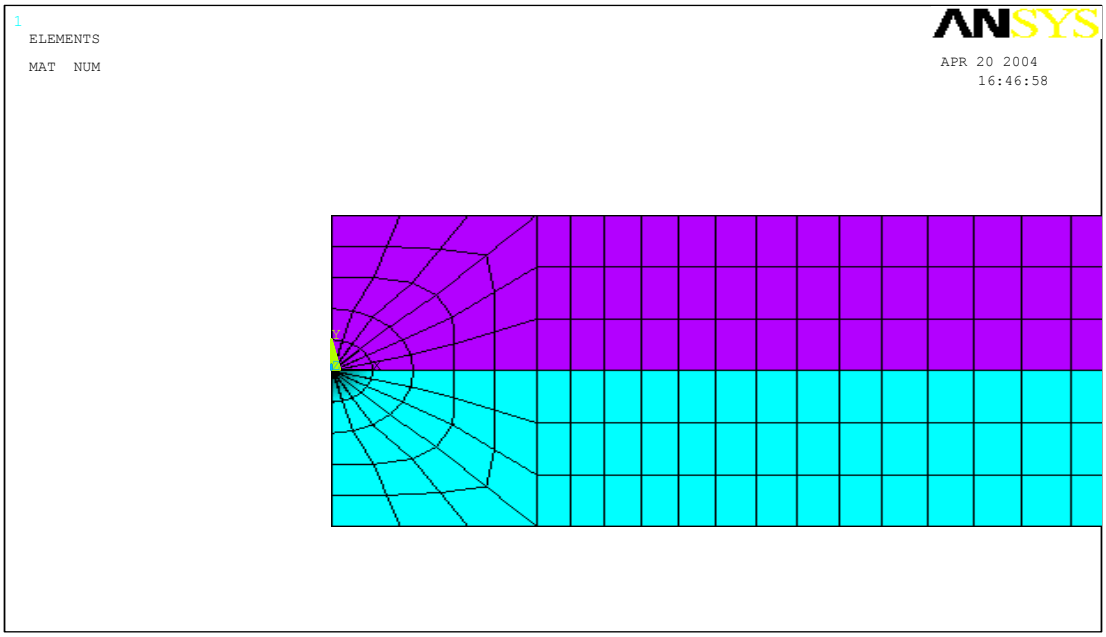

Figure 4.4 Two-dimensional view of the mesh around the vicinity of the crack tip. The crack tip is located at the center of the left-most edge.

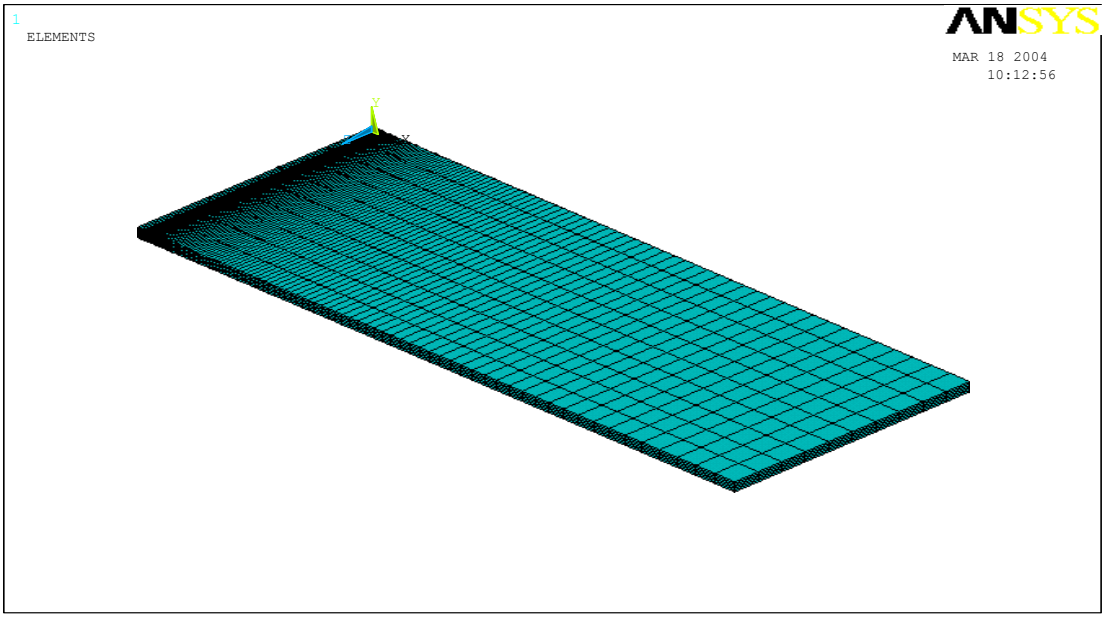

Figure 4.5 Isotropic view of the meshed quarter model. The top view depicts the length and width of the laminate. The microcrack is located on the plane x=0.

4.4 Boundary conditions

Due to symmetry conditions, the nodes on the plane corresponding to y = -0.127mm in figure 4.6, are constrained from moving in the y-direction. (Note here that the origin of the coordinate system is located at the crack tip.) Similarly the nodes on the plane corresponding to z = 2.5 mm are constrained from moving in the z-direction. (This plane is located across the center of the laminate width.) The nodes corresponding to the plane where x = 0 in the upper ply are also constrained in the x-direction. To simulate the microcrack, the nodes on the plane of the lower ply at x = 0 are allowed to move freely in all directions.

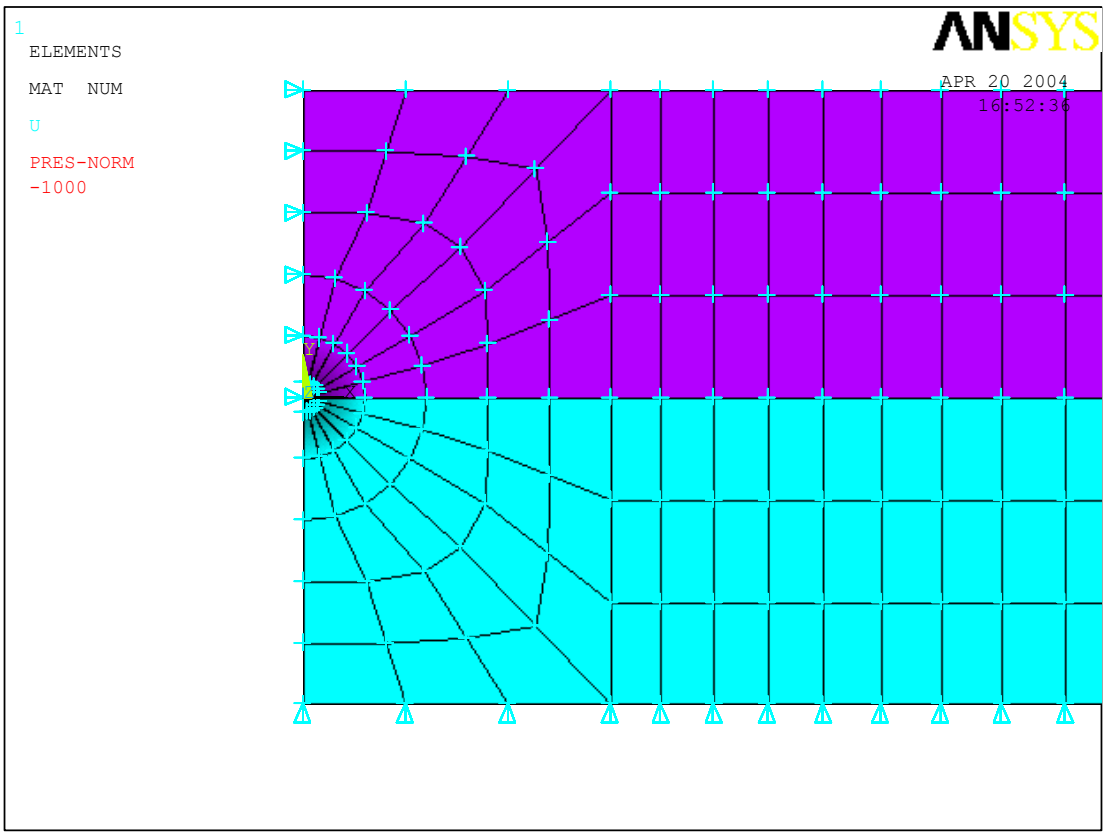

Figure 4.6 Boundary conditions around the vicinity of the microcrack.

4. 5 Loading

It was stated in chapter 3 that complementary research is underway in which a tensile substage is being used to load IM7/977-2 [0/90/90/0] specimens. To simulate this type of uniaxial loading in the finite element model, a pressure load varying from 250 MPa to 1000 MPa is applied at the surface formed by nodes on the plane x = 12.7 mm. This loading condition is shown in figure 4.7.

The magnitude of the loading applied to the laminate must be high enough to obtain substantial out-of-plane displacements at the surface; however, this loading can not be arbitrary. Recall that the goal is to identify microcracking that already exists, not to induce more microcracking. Again, the reference laminate for this work is the [0/90/90/0] laminate used by Larson et al. (1999) [ref 1]. In that work, microcracking was initially identified at a loading of 1100 MPa. Therefore, in the analysis, the highest load on the laminate tested was limited to 1000 MPa.

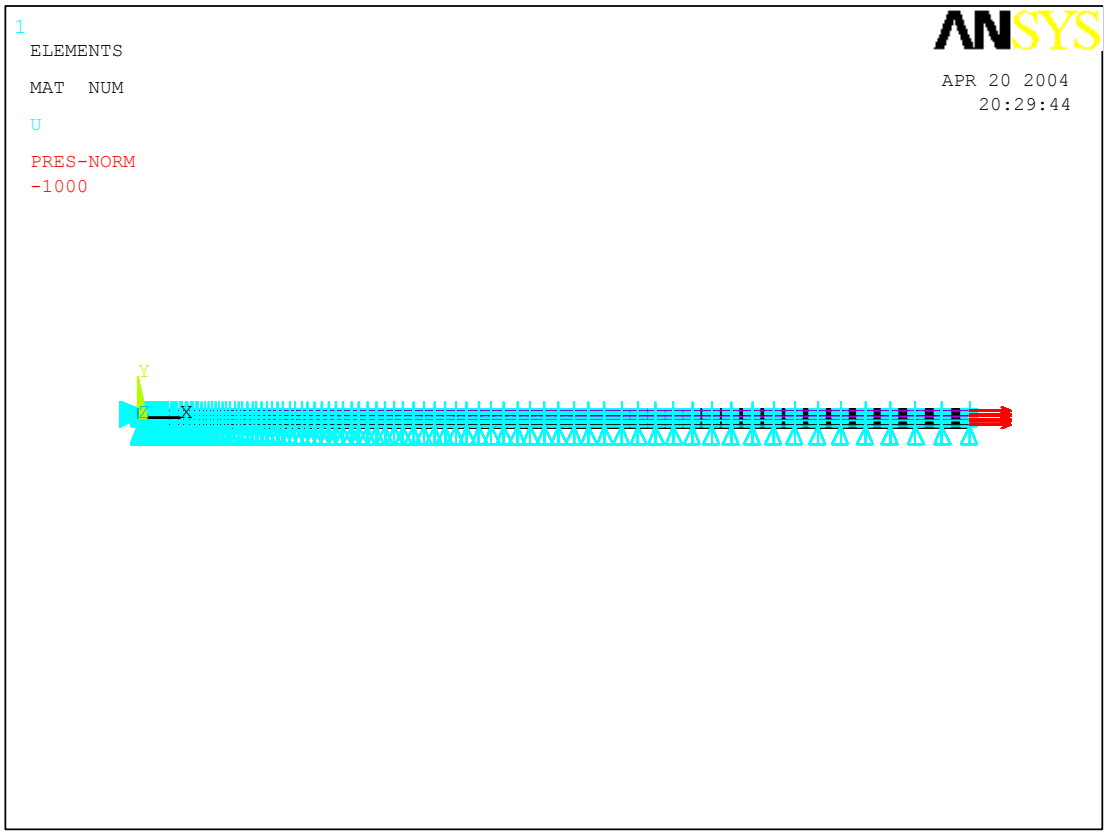

Figure 4.7 Location of force (depicted by red arrows) on the quarter model of the [0/90/90/0] laminate.

4.6 Solution Convergence Testing

Finer meshes were generated for testing the convergence of solution. A finer mesh means more number of elements, which in turn means more degrees of freedom. In this analysis the number of degrees of freedom is increased from 51156 to 80640 for $[0/90]_s$ laminate, at a load of 1000 MPa. Each time *Uy* at the mid-plane is plotted against nodal distance. From figure 4.8 it is evident that the *Uy* solution is converged from along the length of the model for a D.O.F of 51912. Hence for this analysis the number of degrees of freedom used is 51912. When changing the number of degrees of freedom, the nodes at the crack tip in the spider web configuration are changed from four to ten. For each increase in the number of degrees of freedom, the number of elements around the

crack tip are kept equal to the number of nodal divisions at *y*=0 in the spider web. Six nodes at y=0 in the spider web gave same results as 8 nodes and 10 nodes. Hence number of nodes in the spider web and number of elements around the crack tip are taken as six.

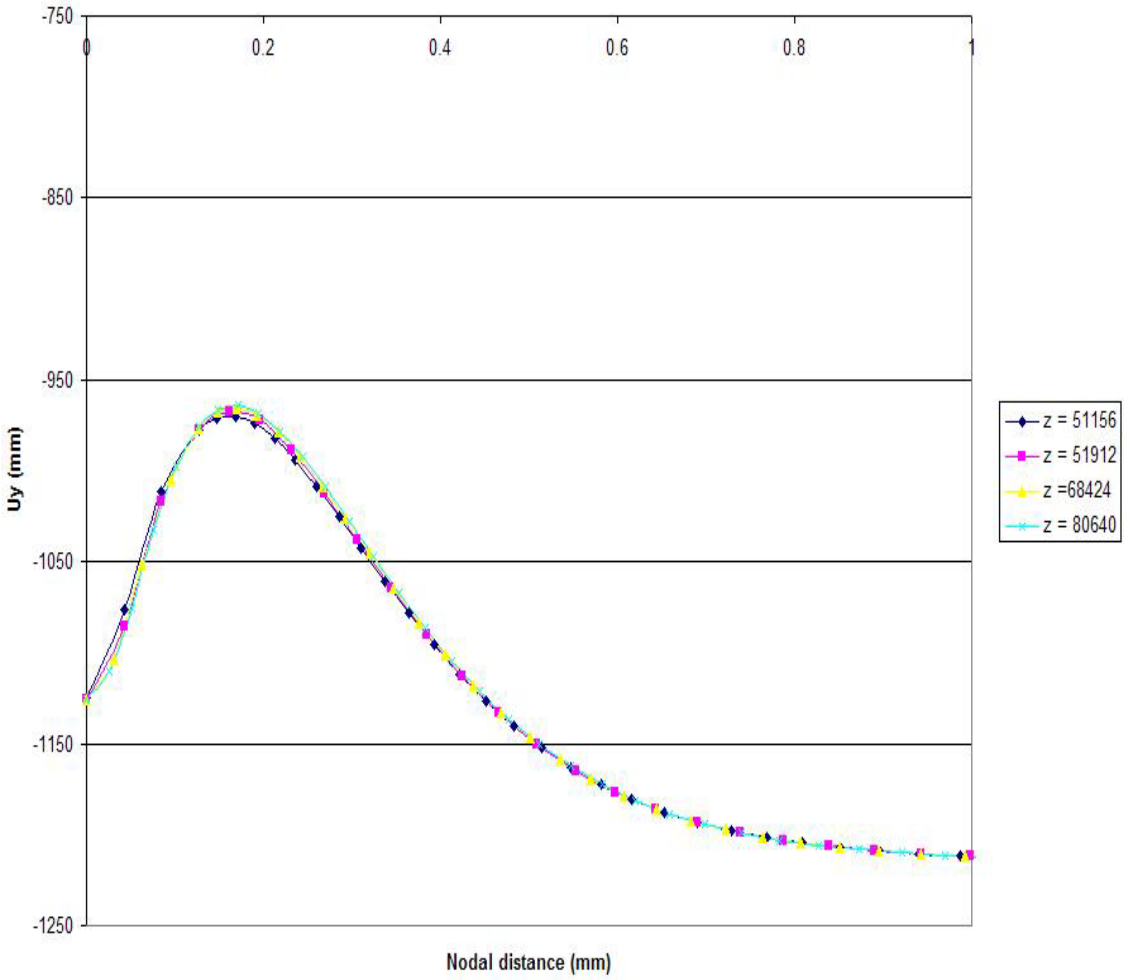

Figure 4.8 Convergence of out-of-pane displacements along the profile plane for the [0/90/90//0] IM7/977-2 laminate loaded to 1000 MPa.

5. Results

Figures 5.1(a) and 5.1(b) show the effect of width on out-of-plane displacements on a section taken near the vicinity of the microcrack for the [0/90/90/0] laminate. The widths of the laminate considered here are 5mm and 10mm. Note for the same 1000MPa loading that edge effects can be observed in both cases. In figures 5.1(a) and 5.1(b) a different displacement contour can be seen at the edges of the laminate, which describes the edge effect. It is evident from the figures that edge effects do not effect the out-of-plane displacements along the *xy* mid-plane.

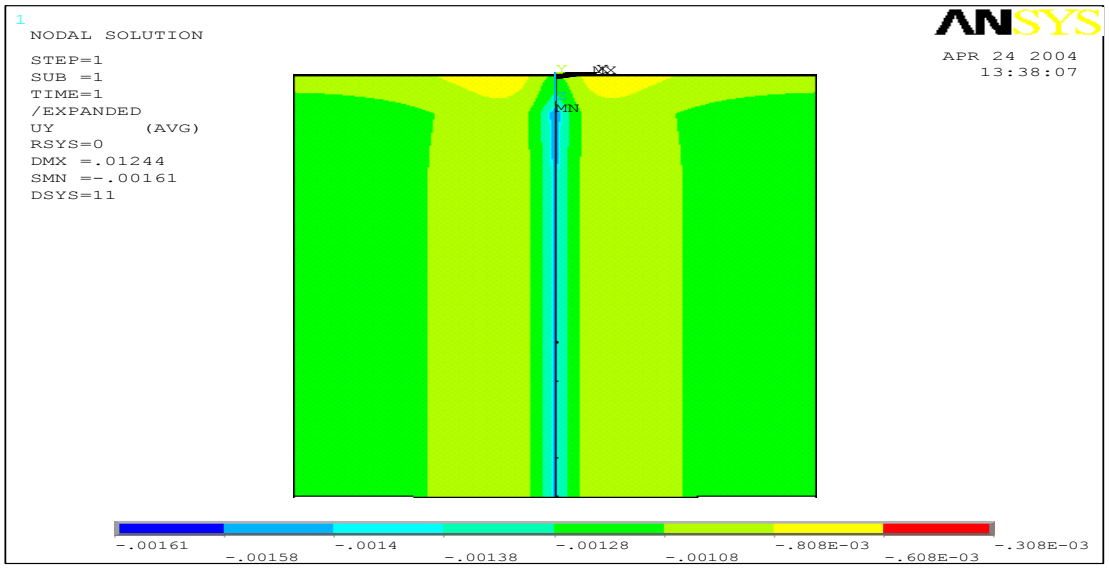

Figure 5.1(a) Out-of plane contours on the top surface of a [0/90/90/0] laminate with a microcrack extending through both 90 plies and a transverse loading of 1000 MPa. This picture shows the top view of a 5mm wide laminate. Here a 2mm section in length is shown with the microcrack located in the center. The top boundary represents the edge of the laminate while the bottom boundary represents the mid-plane. Each contour represents an interval of 100 nanometers.

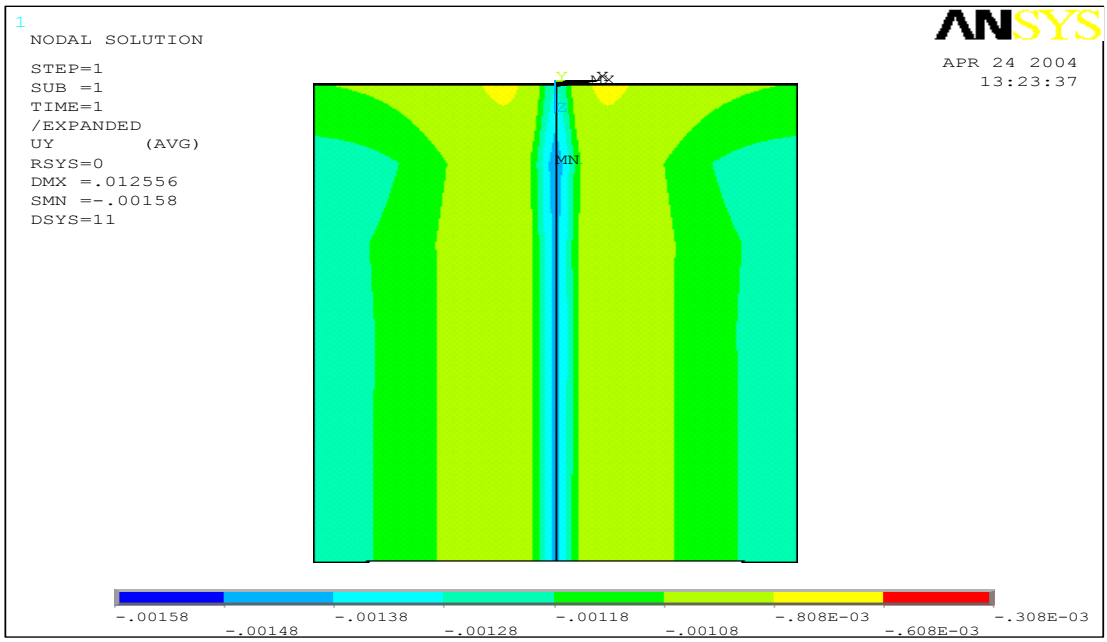

Figure 5.1(b) Out-of plane contours on the top surface of a [0/90/90/0] laminate with a microcrack extending through both 90 plies and a transverse loading of 1000 MPa. This picture shows the top view of a 10 mm wide laminate. Here a 2mm section in length is shown with the microcrack located in the center. The top boundary represents the edge of the laminate while the bottom boundary represents the mid-plane. Each contour represents an interval of 100 nanometers.

The nodal solution for *Uy* (out-of-plane displacement) in the $[0/90]_s$ 5 mm wide laminate along the *xy* mid-plane (located on the plane where z=2.5mm) for a load of 1000 MPa is shown in figure 5.2. In this figure the results have been symmetrically expanded about the *yz* and *xz* planes to show the out-of plane displacements surrounding the microcrack. The figure only shows a 2mm length section of the laminate. In this figure each contour represents an interval of 175 nanometers. In the following analysis, the out-of-plane surface displacements on the *xy* mid-plane are considered for the analysis. This *xy* mid-plane will be referred to as the profile plane.

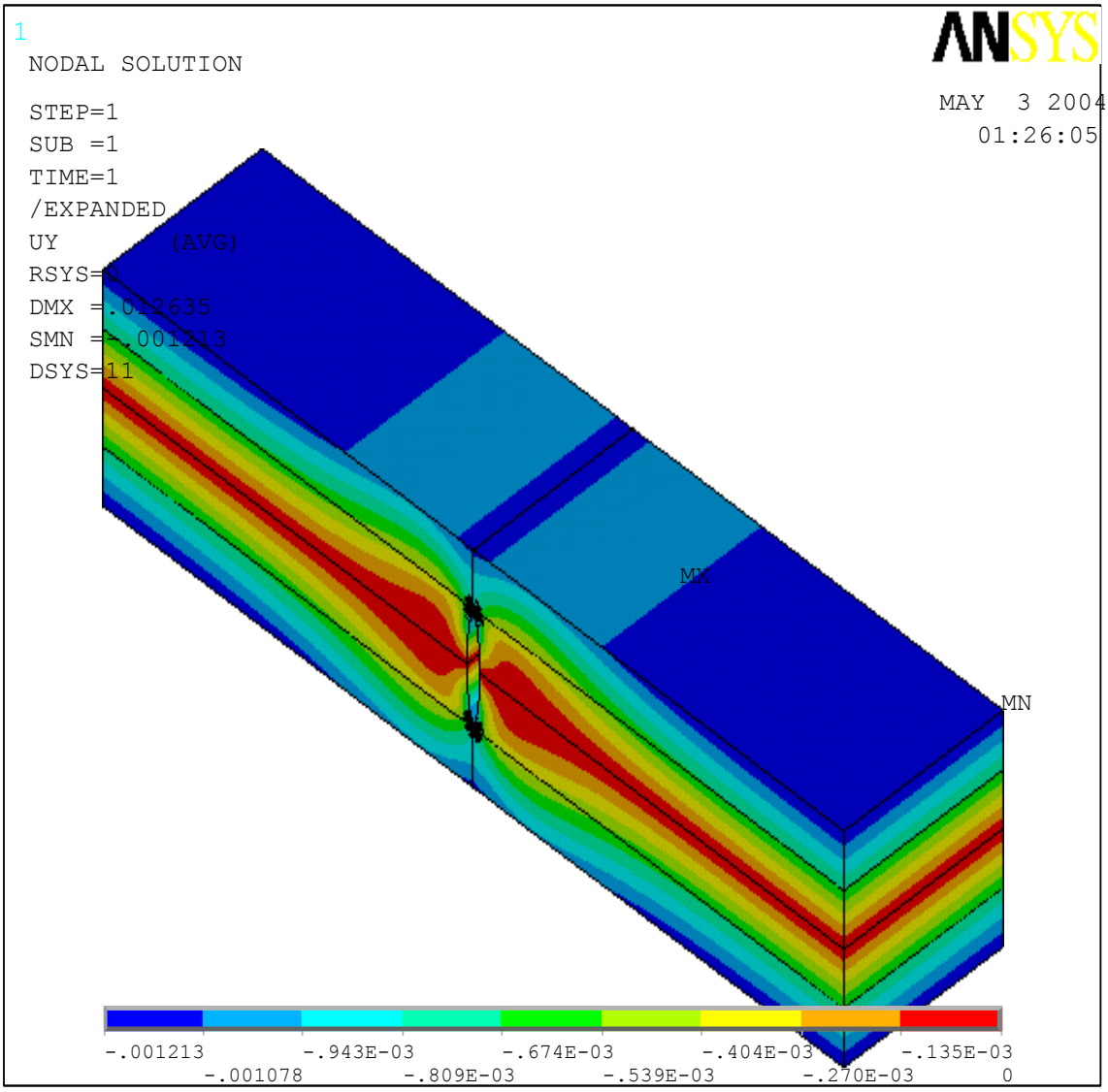

Figure 5.2 *Uy* nodal solution at the *xy* mid-plane for a section length of x = -1 mm to 1 mm for a [0/90/90/0] laminate with a microcrack extending through the 90 plies and a transverse loading of 1000 MPa. In this graph each contour represents 100 nanometers.

In the work performed by Herrington et al. (2002) [ref 13] on penny-shaped cracks in homogeneous materials subjected to a transverse loading, several surface parameters were identified and analyzed with respect to two crack parameters (radius and crack depth). Following this procedure, the surface displacement parameters depicted in figure 5.3 (a) are used in the current analysis. In this figure, $(U_y)_o$ denotes the constant far-field *y*-displacement value, $(U_y)_p$ denotes the peak value, $(U_y)_m$ denotes the minimal value, $(U_x)_p$ denotes the lateral distance of the peak value from the center of the microcrack and $(U_x)_o$ denotes the lateral distance of the constant far-field value from the center of the microcrack. The parameters associated with cracked specimen are a bit more complex due to the heterogeneous nature of the composite laminate. Figure 5.3 (b) denotes the laminate parameters considered in this work. Again, recall that for each case tested the microcrack exists in the center of the specimen and extends through the thickness of the 90º ply group. (It also extends through the entire width.) As shown in the schematic, the half-thickness of the microcrack is represented as *a*. The depth of the microcrack here is considered to be the distance from the laminate surface to the crack tip to the center of the microcrack and is denoted as *d*. Note that for all cases tested this depth is equal to the half-thickness of the laminates. A third parameter d_{ct} denotes the distance from the surface to the crack tip ($d_{ct} = d-a$). Because these laminates are not homogeneous two other parameters dealing with the make-up of the laminate have been identified. The first parameter deals with the ratio of 90º plies to 0º plies and is denoted as *Tp*. For example, for a $[0/90]_s$ laminate the ratio is 1/1 and for a $[0/0/0/90]_s$ the ratio is 1/3. The second parameter deals with the ratio of 90º plies to 0º plies in the d_{ct} region and is denoted as

Dp. (In figure 5.3 (b) the d_{ct} region is highlighted in yellow.) For example, for a $[0/90]_s$ laminate, *Dp*=0, and for a $[0/90/0/90]_s$ laminate *Dp*=1/2.

Eleven different IM7/977-2 cross-ply laminate configurations were analyzed in this research. Recall from chapter 4 that each ply has a constant thickness of t = 0.127mm. The mesh for the $[0/90]_s$ laminate is depicted in figure 4.4. This reference mesh was used in each of the other ten meshes to be the mesh around the crack tip.

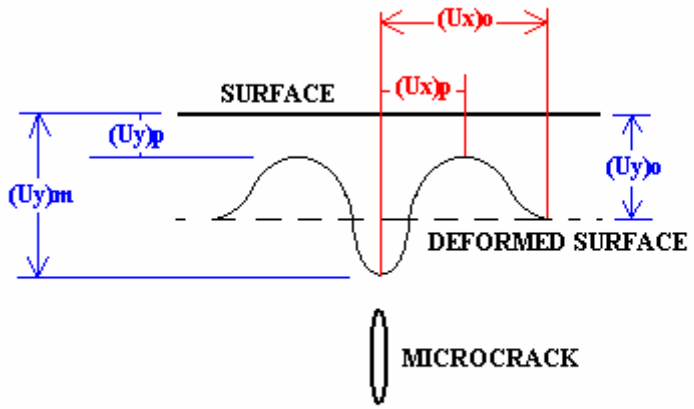

(a)

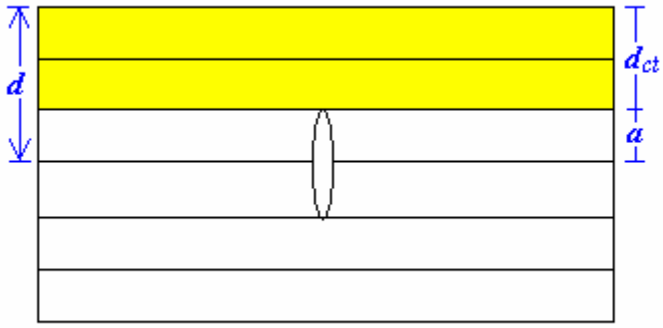

(b)

Figure 5.3 (a) Schematic defining surface parameters. (b) Schematic defining laminate parameters.

When adding outer plies to the finite element geometry, nodes on the top surface of the reference mesh are copied that many times depending on number of plies and are joined by rectangular elements. A similar procedure is followed for adding more inner plies, using the bottom surface of the reference mesh. Meshes used for $[0/0/90]_s$ and $[0/90/90]_s$ are shown in figures 5.4(a) and 5.4(b). The boundary conditions, material properties, and loading conditions are also modified each time to reflect the appropriate behavior of the laminate. For each laminate transverse loadings of 250MPa, 500MPa, 750 MPa, and 1000 MPa were applied. Table I summarizes the resulting surface data in terms of the parameters shown in Figure 5.3.

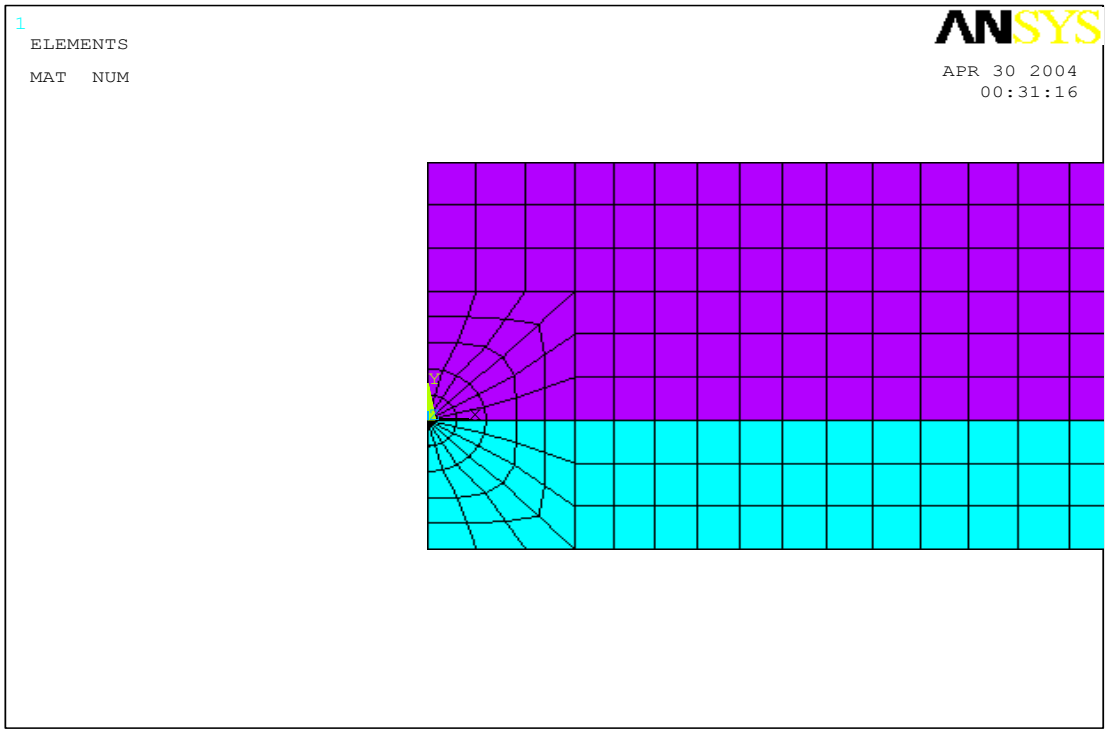

Figure 5.4 (a) Mesh of the $[0/0/90]_s$ laminate.

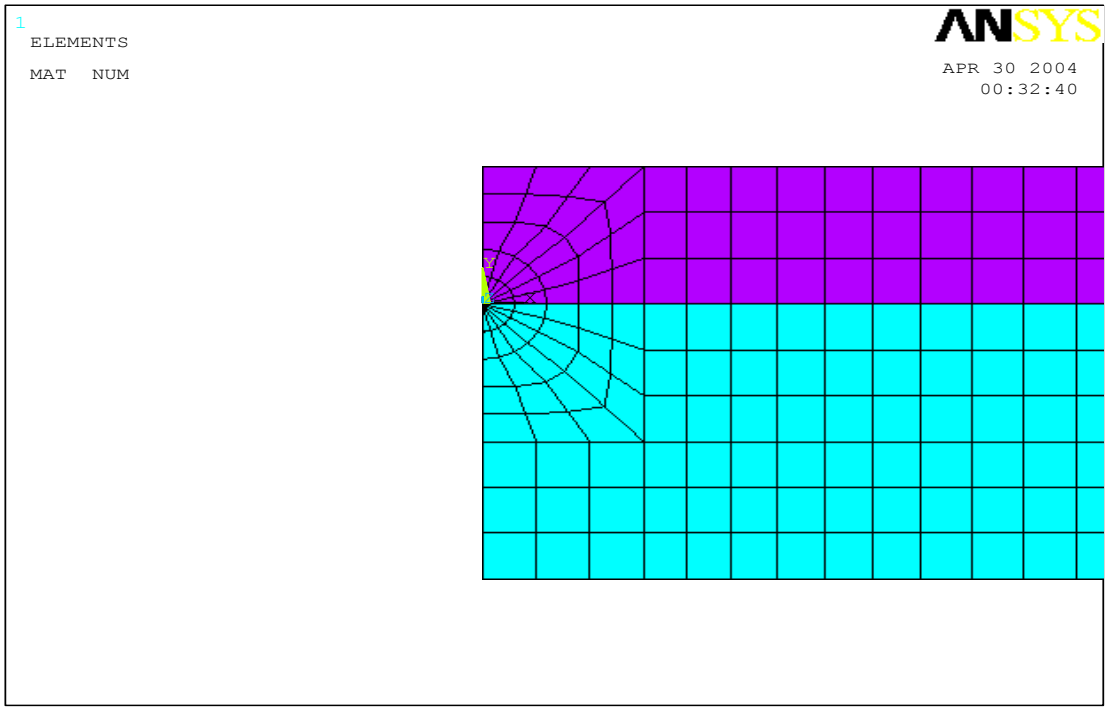

Figure 5.4 (b) Mesh of the $[0/90/90]_s$ laminate.

Table I. Surface Parameter Values for Different Ply Orientations and Loadings.

Laminate Number	Ply Orientation	Loading (MPa)	$(Ux)_p$ (mm)	$(Uy)_p$ (nm)	$(Uy)_m$ (nm)	$(Uy)_p$–$(Uy)_m$ (nm)	$(Uy)_o$ (nm)	$(Ux)_o$ (mm)
1	$[0/90]_s$	250	0.16	-242	-282	40	-303	0.55
	a=t d=2t	500	0.16	-483	-563	80	-607	0.55
	d_{ct}=t	750	0.16	-726	-844	118	-910	0.55
	Tp=1 Dp=0	1000	0.16	-968	-1126	158	-1214	0.55
2	$[0/90/90]_s$	250	0.31	-454	-725	271	-676	1.05
	a=2t d=3t	500	0.31	-907	-1451	544	-1352	1.05
	d_{ct}=t	750	0.31	-1361	-2176	815	-2027	1.05
	Tp=2 Dp=0	1000	0.31	-1814	-2901	1087	-2703	1.05
3	$[0/90/90/90]_s$	250	0.42	-687	-1430	743	-1165	1.49
	a=3t d=4t	500	0.42	-1373	-2860	1487	-2331	1.49
	d_{ct}=t	750	0.42	-2060	-4290	2230	-3496	1.49
	Tp=3 Dp=0	1000	0.42	-2746	-5720	2974	-4662	1.49
4	$[0/90/90/90/90]_s$	250	0.55	-937	-2398	1461	-1755	1.92
	a=4t d=5t	500	0.55	-1874	-4796	2922	-3510	1.92
	d_{ct}=t	750	0.55	-2811	-7194	4383	-5266	1.92
	Tp=4 Dp=0	1000	0.55	-3748	-9592	5844	-7020	1.92
5	$[0/0/90]_s$	250	0.16	-296	-303	7	-333	0.51
	a=t d=3t	500	0.16	-593	-606	13	-666	0.51
	d_{ct}=2t	750	0.16	-890	-909	19	-999	0.51
	Tp=1/2 Dp=0	1000	0.16	-1186	-1211	25	-1332	0.51
6	$[0/0/0/90]_s$	250	0.13	-357	-358	1	-386	0.42
	a=t d=4t	500	0.13	-714	-716	2	-771	0.42
	d_{ct}=3t	750	0.13	-1071	-1073	2	-1156	0.42
	Tp=1/3 Dp=0	1000	0.13	-1428	-1431	3	-1541	0.42
7	$[0/0/0/0/90]_s$	250	-	-418	-418	0	-442	0.30
	a=t d=4t	500	-	-836	-836	0	-884	0.30
	d_{ct}=3t	750	-	-1254	-1254	0	-1326	0.30
	Tp=1/4 Dp=0	1000	-	-1671	-1671	0	-1770	0.30

Laminate Number	Ply Orientation	Loading (MPa)	$(Ux)_p$ (mm)	$(Uy)_p$ (nm)	$(Uy)_m$ (nm)	$(Uy)_p$–$(Uy)_m$ (nm)	$(Uy)_o$ (nm)	$(Ux)_o$ (mm)
8	$[90/0/0/90]_s$	250	0.16	-564	-566	2	-607	0.30
	a=t d=4t	500	0.16	-1128	-1132	4	-1214	0.30
	d_{ct}=3t	750	0.16	-1692	-1698	6	-1821	0.30
	Tp=1 Dp=1/2	1000	0.16	-2256	-2264	8	-2428	0.30
9	$[90/0/90]_s$	250	0.16	-605	-623	18	-676	0.38
	a=t d=3t	500	0.16	-1212	-1247	35	-1352	0.38
	d_{ct}=2t	750	0.16	-1818	-1870	52	-2028	0.38
	Tp=2/3 Dp=1	1000	0.16	-2423	-2494	71	-2704	0.38
10	$[0/0/90/90]_s$	250	0.34	-484	-565	81	-607	1.05
	a=2t d=4t	500	0.34	-968	-1130	162	-1214	1.05
	d_{ct}=2t	750	0.34	-1451	-1695	244	-1821	1.05
	Tp=1 Dp=0	1000	0.34	-1935	-2260	325	-2428	1.05
11	$[0/90/0/90]_s$	250	0.12	-566	-567	1	-607	0.38
	a=t d=4t	500	0.12	-1131	-1134	3	-1214	0.38
	d_{ct}=3t	750	0.12	-1697	-1701	4	-1821	0.38
	Tp=1 Dp=1/2	1000	0.12	-2252	-2267	15	-2428	0.38

Far-field Uy Values

When comparing the far-field *y*-displacement values for all eleven cases in Table I for any given load the biggest deformation occurs in case 4 for a [0/90/90/90/90] laminate and the smallest value occurs in case 1 for a [0/90]s laminate. It is obvious from the table that the values are dependent on the laminate thickness, *d*, as well as the ratio of 90º plies to 0º plies. This trend is expected since the far-field *y*-value is dependent on laminate geometry and not the microcrack. For cases 2 and 9 the far-field values are equal. This is expected since both laminates have the same laminate thickness and the same number of 0º and 90º plies. The same is true for cases 8, 10, and 11. Also, note that for these cases the far-field value is 2430 nm, which is twice that of case 1. This is also

expected since the number of plies is doubled for these cases and the ratio of 90º plies to 0º plies remained constant. As expected, an increase in the laminate thickness will result in a larger displacement after Poisson's contraction. Also, as expected, the 90º plies influence the surface deformation more greatly because (1) the Poisson's contraction in this *xy* plane is greater and (2) the stiffness in the *y*-direction is much less. Because this contraction is constant over the surface, this value is subtracted from the profile caused by the presence of the microcrack in subsequent graphs.

Minimal Values

The graph in figure 5.5 displays *Uy* displacements on the profile plane for $[0/90]_s$, $[0/90/90]_s$, $[0/90/90/90]_s$ and $[0/90/90/90/90]_s$ laminates at a load of 1000 MPa. Recall that for these cases the depth of the crack tip below the surface, d_{ct}, is a constant value of 0.127mm. However, the half-length of the microcrack, *a*, is increased from *t* to *4t*; as a result the laminate thickness is also increasing. It is evident from the graph that as *a* increases the minimal value also increases in distance from the peak value. Note that for all of the cases except $[0/90]_s$, the minimal value is below 0. This physically represents that the surface pulls in above the plane of the microcrack.

The graph in figure 5.6 displays *Uy* displacements on the profile plane for $[0/90]_s$, $[0/0/90]_s$, $[0/0/0/90]_s$ and $[0/0/0/0/90]_s$ laminates at a load of 1000 MPa. For these cases the microcrack length *a* is a constant value of 0.127mm and the crack tip depth, d_{ct}, is increased from *t* to *4t*. As d_{ct} is increased, the minimal value decreases in magnitude.

Location of Peak Values

The lateral peak distance is shown in Table I for each case. Because the nodal spacing along the profile plane is a maximum of 0.03mm, the values

listed are only accurate to ±0.03mm. From figure 5.5 it is evident that the location of the maximum peak moves away from the center of the microcrack as the microcrack length is increased. In figure 5.6 it appears that the lateral distance to the peaks decreases as the depth of the microcrack below the surface increases.

Since the size of the microcrack is changing as the laminate thickness is increasing (and the depth of the center of the crack) perhaps a figure in which the laminate thickness is a constant would help in decoupling these parameters. The graph in figure 5.7 gives the displacement profile comparison among the $[0/0/90]_s$, $[0/90/90]_s$, and $[90/0/90]_s$ laminates. Note that the total thickness of three laminates is kept constant and displacements at 1000 MPa load are compared. While the location of the peak value for the $[0/0/90]_s$, and $[90/0/90]_s$ appear to be similar, the $[0/90/90]_s$ laminate appears to have a peak value farther away from the crack tip. Similarly, the graph in Figure 5.8 shows the comparison of *Uy* displacements for $[0/0/0/90]_s$, $[0/0/90/90]_s$, $[0/90/90/90]_s$, $[0/90/0/90]_s$ laminates at a load of 1000 MPa. When examining the laminates with $a=2t$ and $a=3t$ it is obvious that as the microcrack length is increased the distance to the peak value increases.

Difference in Peak and Minimal Values

From figure 5.5 it is evident that the maximum peak value increases as the microcrack length below the surface is increased; the difference between peak and minimal values also increase with an increase in microcrack length. Figures 5.9 and 5.10 depict how the peak values and the difference in peak and minimal values changes with an increase in microcrack length when the outer plies are all 0; i.e., $Dp=0$. Refer to Case A in the graphs. Note the strong dependence on the size of the microcrack and the

difference in peak and minimal values. Figures 5.9 and 5.10 also depict how the peak values and the difference in peak and minimal values changes with an increase in depth of the crack tip when the outer plies are all 0; i.e., *Dp*=0. Refer to Case B in the graphs. For this series of laminates the difference in peak and minimal values tended to zero as the depth of the crack tip was increased. This trend can be seen clearly in Figure 5.6. When the depth of the crack tip became four times greater than the half-length of the crack the displacement profile no longer pinched in above the plane of the crack. From the comparison of $[0/0/90]_s$, $[0/90/90]_s$, and $[90/0/90]_s$ laminates in figure 5.7, the maximum difference occurs for a $[0/90/90]_s$ laminate and the minimum for a $[0/0/90]_s$ laminate. The $[0/90/90]_s$ laminate should yield the maximum difference when loaded due to the fact that it has a larger microcrack located closer to the surface. Although the $[0/0/90]_s$ and $[90/0/90]_s$ laminates both have microcracks of the same thickness and depth, the $[90/0/90]_s$ laminate yields more of a difference in displacements upon loading because the 90º ply on the outer surface is more compliant than the 0º ply on the outer surface. Figure 5.11 displays the displacement pattern for $[0/90]_s$ and $[0/0/90/90]_s$ laminates. Note that as expected, the difference in values is doubled.

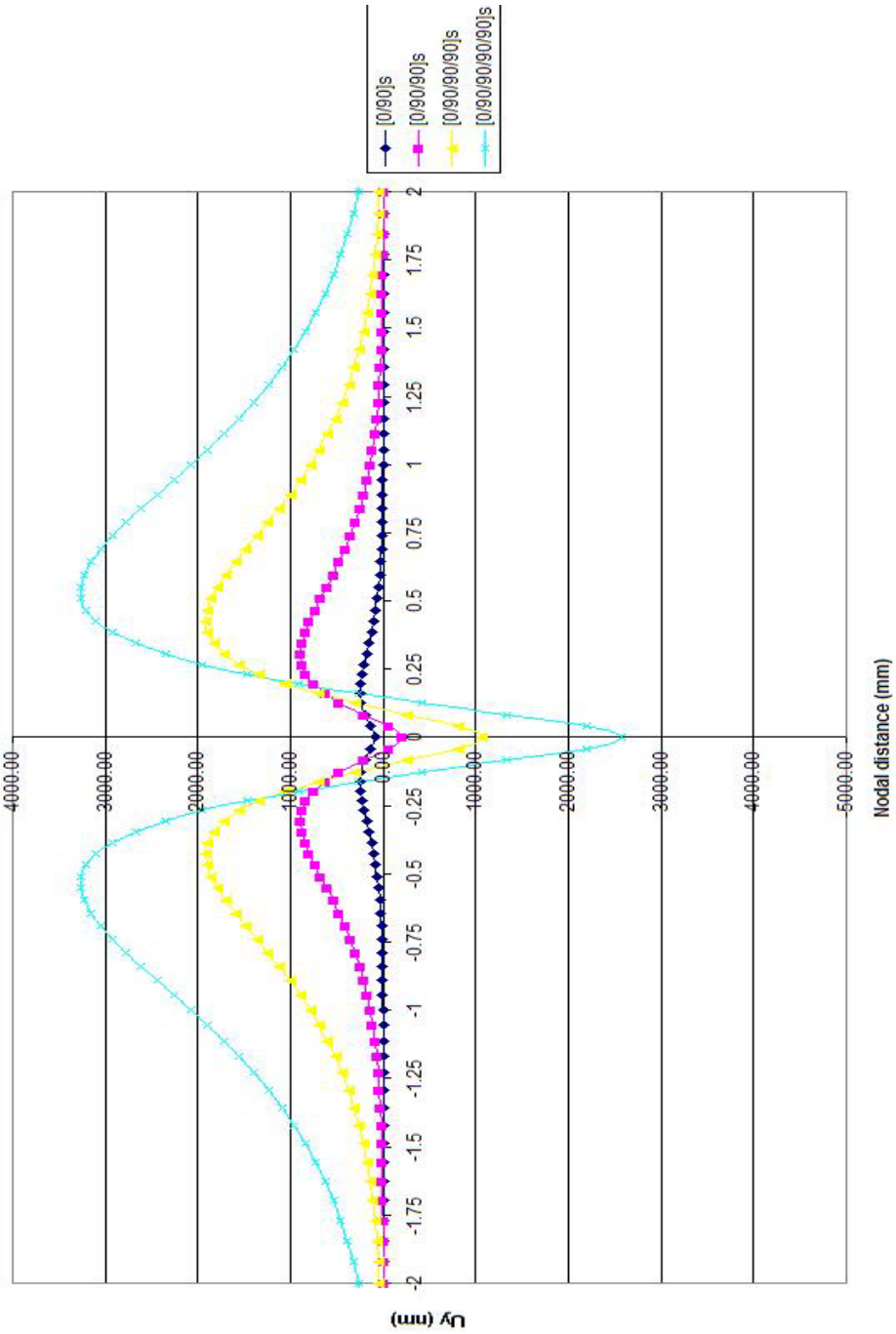

Figure 5.5 *Uy* displacements along profile plane for four cross-ply transversely loaded to 1000 MPa. For each consecutive case, the microcrack length is the increasing. The depth of the crack below the surface is kept constant. (The far-field *Uy* displacements have been subtracted from the profile.)

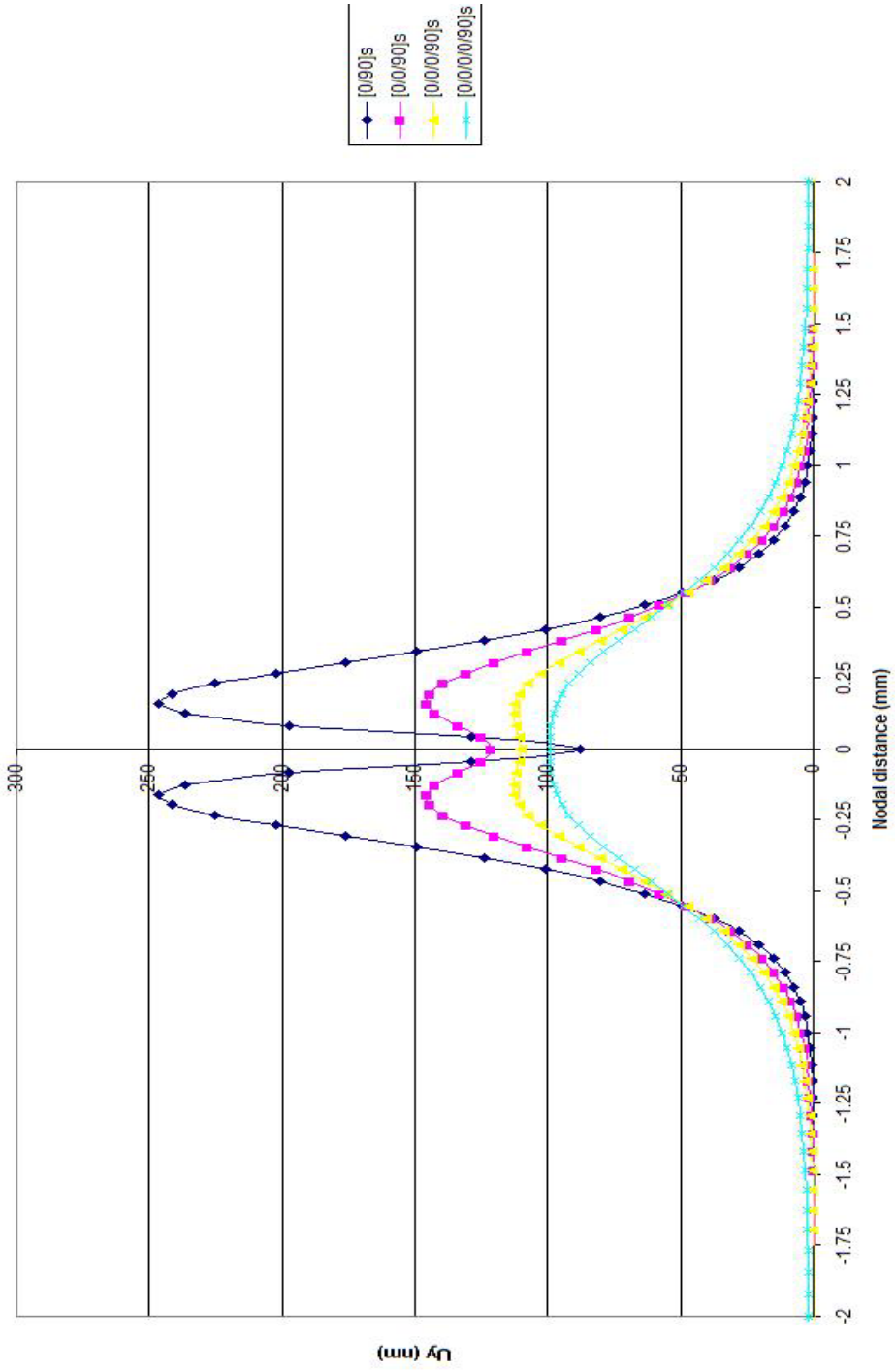

Figure 5.6 *Uy* displacements along profile plane for four cross-ply transversely loaded to 1000 MPa. For each case, the microcrack length is the same. The depth of the crack below the surface is varied. (The far-field *Uy* displacements have been subtracted from the profile.)

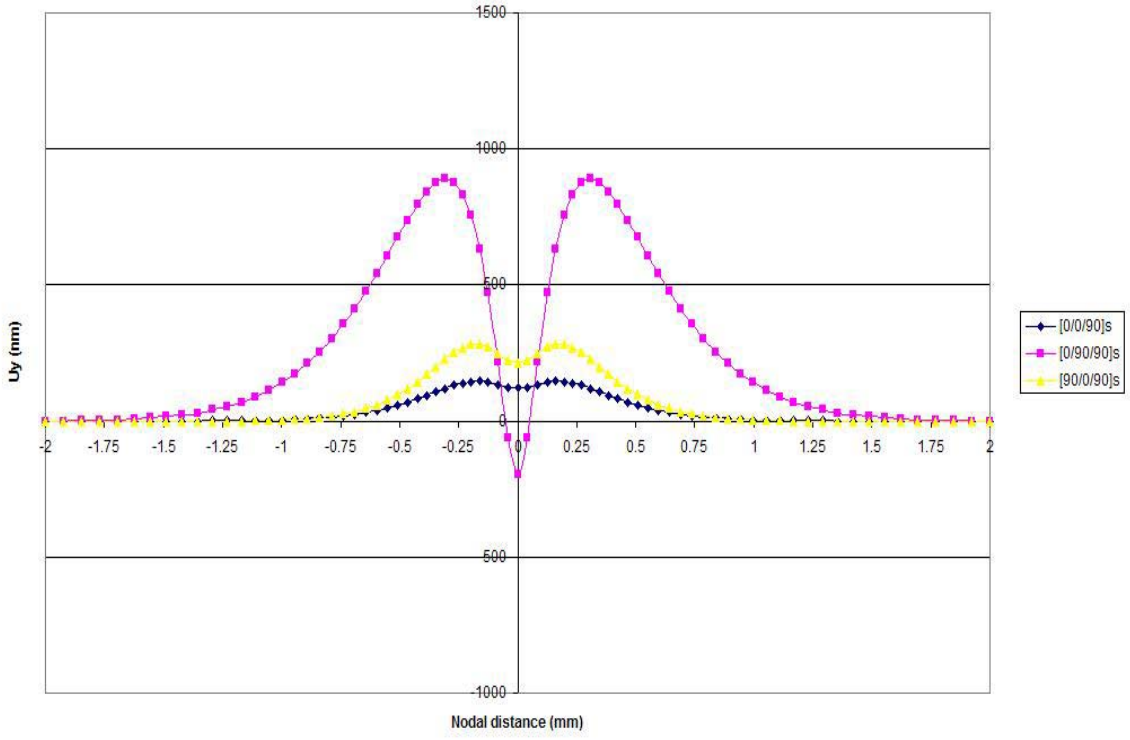

Figure 5.7 *Uy* displacements along profile plane for cross-ply laminates totaling a laminate thickness of *6t* transversely loaded to 1000 MPa. (The far-field *Uy* displacements have been subtracted from the profile.)

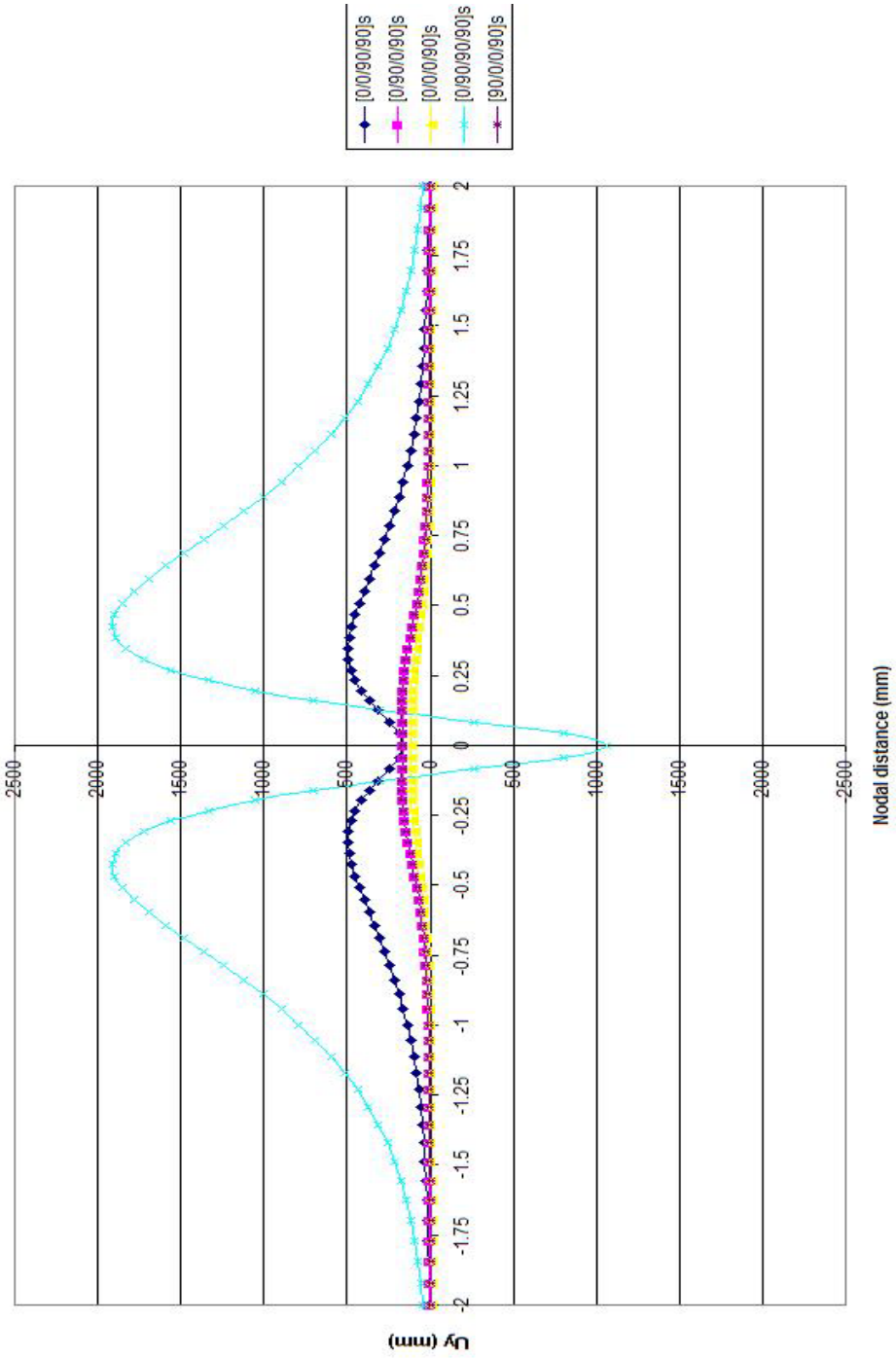

Figure 5.8 *Uy* displacements along profile plane for cross-ply laminates totaling a laminate thickness of *8t* transversely loaded to 1000 MPa. (The far-field *Uy* displacements have been subtracted from the profile.)

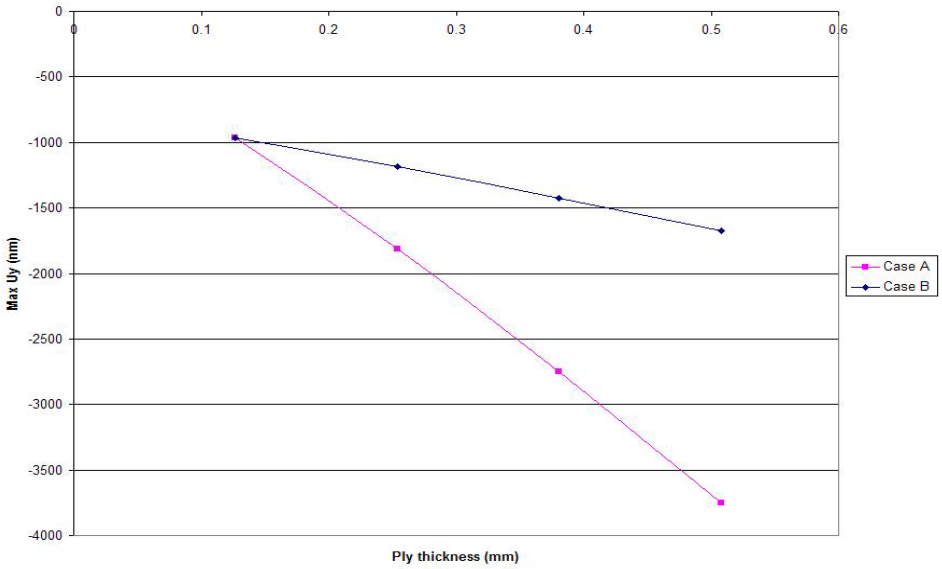

Figure 5.9 Graph showing variation of maximum peak value for a load of 1000MPa. Case A represents four laminates with crack tips the same distance below the surface. The microcrack length varies according to ply thickness as shown. Case B represents four laminates having the same size microcrack. The depth of the crack tip below the surface varies with ply thickness as shown.

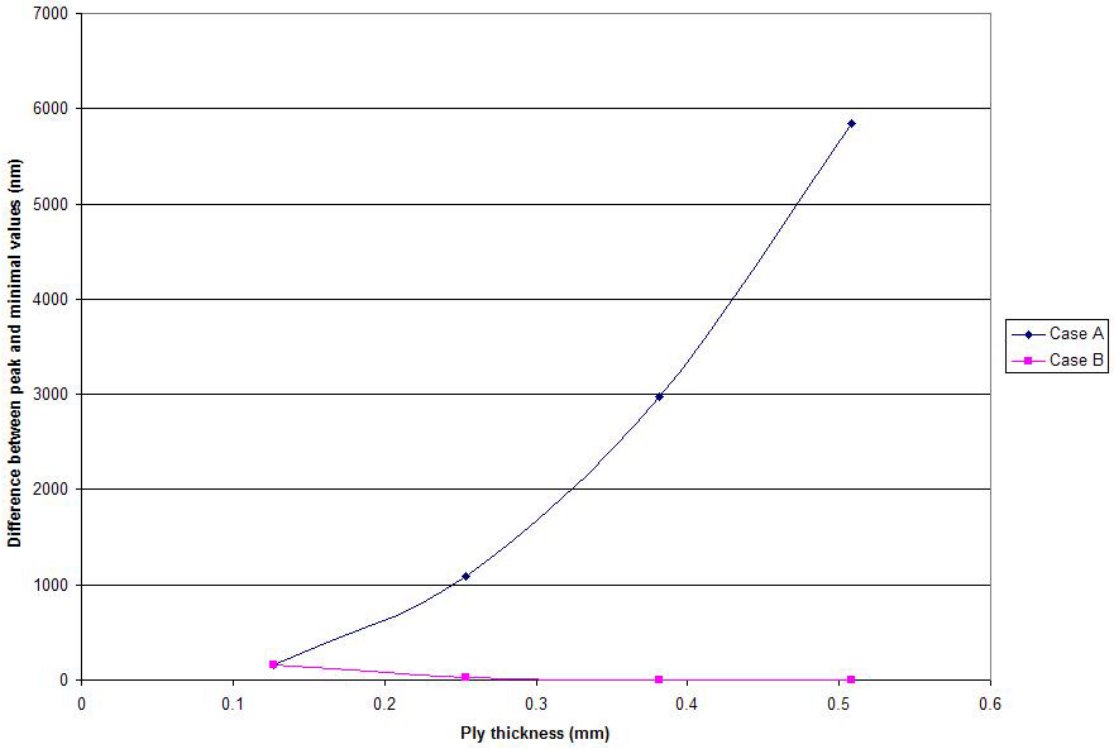

Figure 5.10 Graph showing variation of difference between peak and minimal values. Case A represents four laminates with crack tips the same distance below the surface. The microcrack length varies according to ply thickness as shown. Case B represents four laminates having the same size microcrack. The depth of the crack tip below the surface varies with ply thickness as shown.

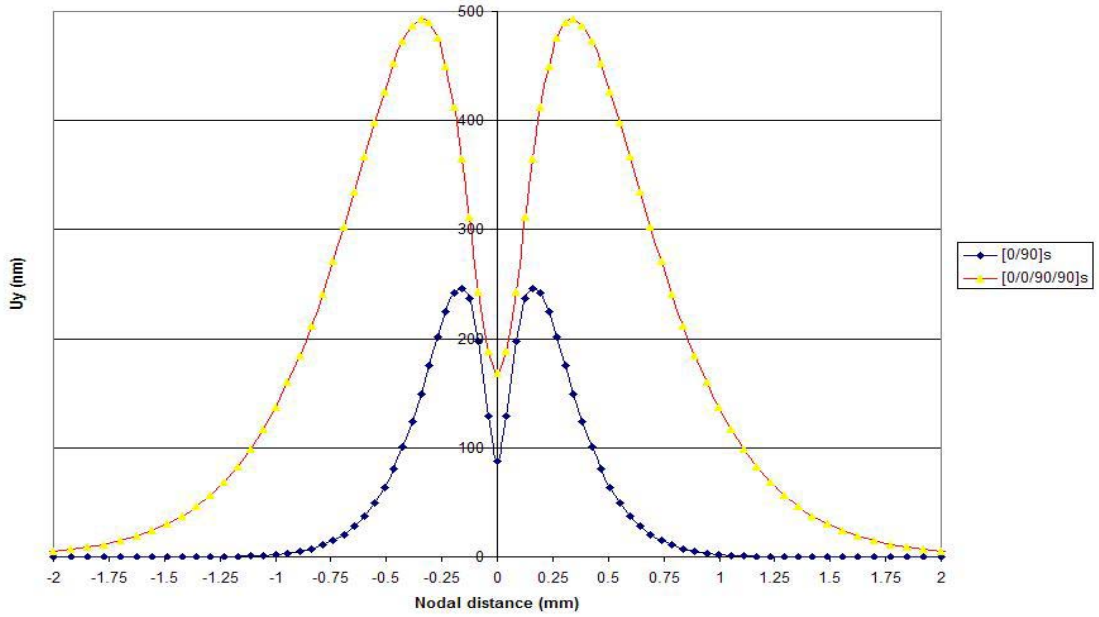

Figure 5.11 Comparison of *Uy* displacements for $[0/90]_s$ and $[0/0/90/90]_s$ laminates. (The far-field *Uy* displacements have been subtracted from the profile.)

Lateral Distance to Uy far-field Value

The lateral distance to the far-field value is taken to be the *x*-distance where the out-of-plane displacement is within 5% of the far-field value. These far-field values and the lateral distances to the far-field values are listed in Table I. From figure 5.5 it is evident that the lateral distance of the far-field value is increasing with the microcrack length. From figure 5.6 it can be observed that the lateral distance of the far-field value is decreasing with an increase in d_{ct}. In figure 5.7 a larger far-field lateral distance is seen in the case of $[0/90/90]_s$ laminate. Because D_p is larger for a $[90/0/90]_s$ laminate when compared to a $[0/0/90]_s$ laminate, less lateral distance can be seen for $[90/0/90]_s$ laminate. From figure 5.8 it is evident that as the size of the microcrack increases, although the depth of the center of the crack remains constant, the lateral distance to the far-field value increases. As d_{ct} is more and a is less for a $[0/0/0/90]_s$

laminate, it takes less lateral distance to reach the far-field value. As d_{ct}, $T_{p,}$ and D_p are all the same for $[0/90/0/90]_s$ and $[90/0/0/90]_s$ laminates, the same lateral far-field distance can be observed.

Influence of Loading

As shown in Table I, the pressure loading has a linear relationship to the *Uy* displacement values. Also shown in the table, the loading does not effect the peak location of the *Uy* values. It also has no effect on the location of the far-field value.

Discussion of Displacement Profiles

The difference in the *Uy* values is the main indicator whether or not the magnitude of displacements is sufficient for an optical technique to resolve. Figures 5.12(a), 5.12(b) and 5.12(c) yield the *Uy* displacement contours on the top surface of the $[0/90]_s$, $[0/90/90]_s$, and $[0/0/90/90]_s$ IM7/977-2 laminates subjected to a transverse loading of 1000 MPa. From these figures, it appears that an optical technique does have the potential of identifying microcracking if its resolving power is within 100 nanometers. In comparing these three laminate configurations, microcracking in the $[0/90/90]_s$ laminate would intuitively be easier to identify because of the larger displacement profile.

Another consideration is spatial resolution. In all of these cases the displacement profiles are all contained within a few millimeters of the length of the laminate. For example, for the $[0/90]_s$ laminate loaded to 1000 MPa, the difference in the peak and minimal values is 158 nanometers and occurs within a lateral distance of 0.16 mm. If each fringe represented a contour of 50 nm, the lens must be powerful enough to resolve 3 fringes in the 0.16mm distance. Similarly, the difference in peak and far-field

values is 246 and occurs in a lateral distance of 0.39 mm. Therefore, if each fringe represented a contour of 50 nm, the lens must be powerful enough to resolve 4 fringes in the 0.39mm distance. Obviously, the lens required to resolve the fringes in the latter case would not have to be as powerful as the lens required in the former case. Figure 5.13 depicts these two regions. The region from the center of the microcrack to the peak value is defined as region A and the region between the peak and constant far-field values is defined as region B. The difference in peak and minimal values is defined by A_y while A_x represents the lateral distance to the peak value. Similarly, B_y is the difference between the peak and far-field values while B_x represents the lateral distance between peak and far-field values. Tables II, III, IV and V displays the *Ax*, *Ay*, *Bx* and *By* values for different ply orientations at a transverse loading of 1000 MPa.

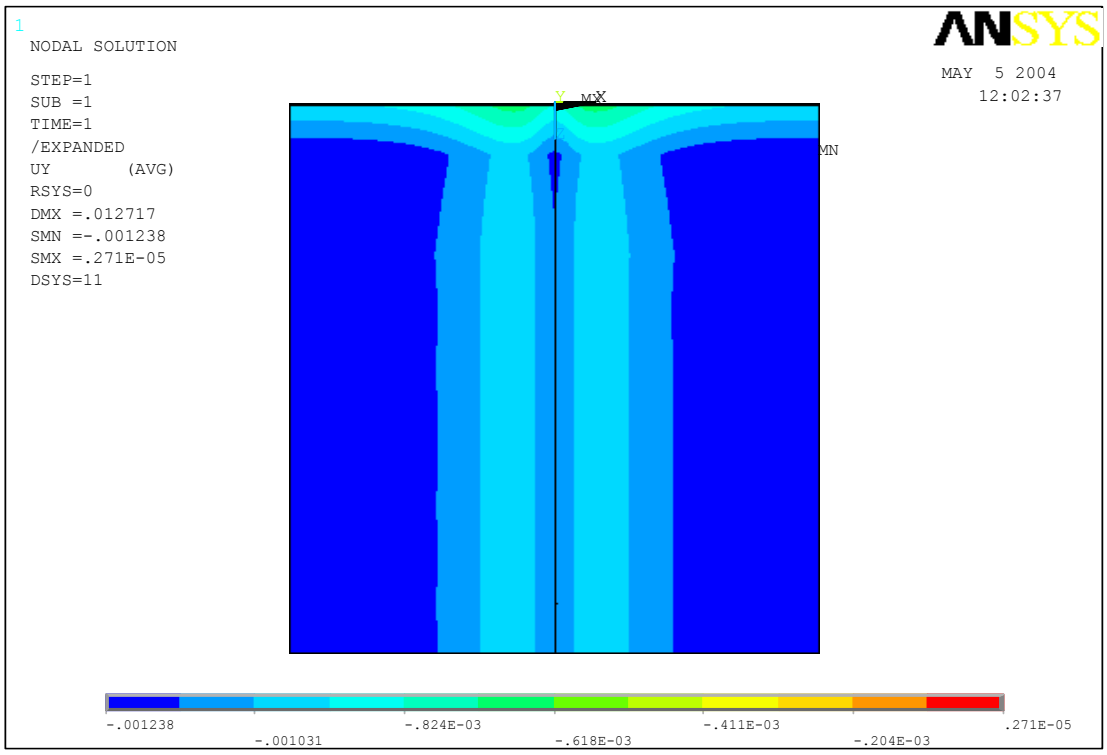

Fig 5.12(a) *Uy* displacement pattern for a section length of x = -1 mm to 1 mm for a [0/90/90/0] laminate with a microcrack extending through the 90 plies and a transverse loading of 1000 MPa.

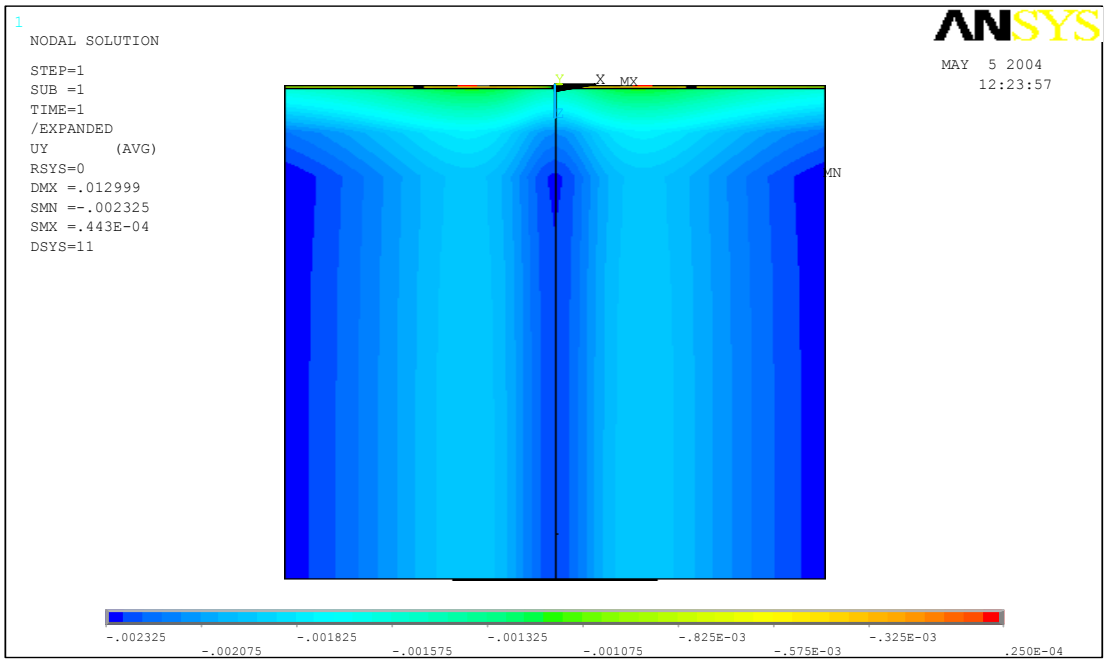

Fig 5.12(b) *Uy* displacement pattern for a section length of x = -1 mm to 1 mm for a [0/90/90/90/90/0] laminate with a microcrack extending through the 90 plies and a transverse loading of 1000 MPa.

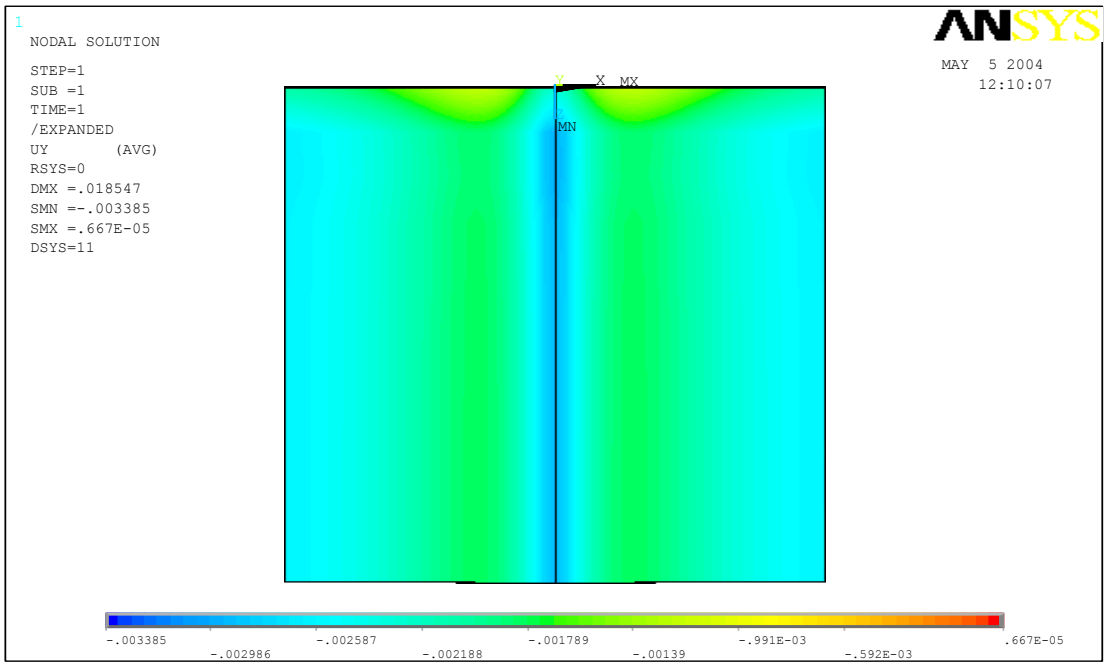

Fig 5.12(c) *Uy* displacement pattern for a section length of x = -1 mm to 1 mm for a [0/0/90/90/0/0] laminate with a microcrack extending through the 90 plies and a transverse loading of 1000 MPa.

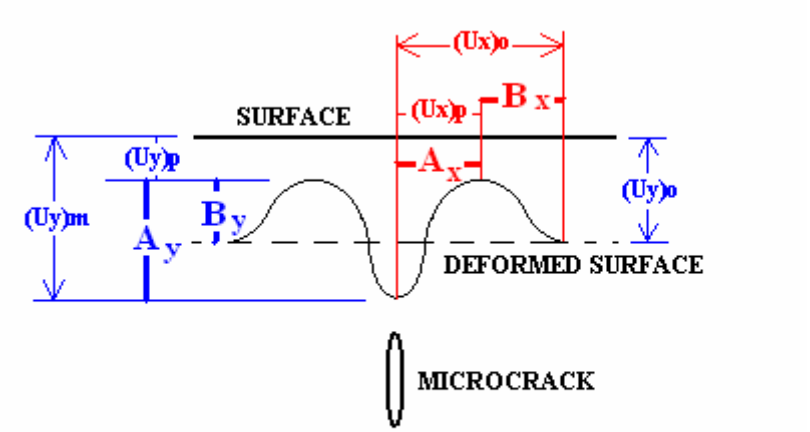

Figure 5.13 Schematic showing Regions A and B.

Table II. Surface Parameter Values for Laminates with d_{ct} = t and loading = 1000 MPa.

LAMINATE	*Ay* *(nm)*	*Ax* *(mm)*	*By* *(nm)*	*Bx* *(mm)*
[0/90]	158	0.16	246	0.39
[0/90/90]	1087	0.31	889	0.74
[0/90/90/90]	2974	0.42	1916	1.07
[0/90/90/90/90]	5844	0.55	3272	1.37

Table III. Surface Parameter Values for Laminates with *a* = t and loading = 1000 MPa.

LAMINATE	*Ay* *(nm)*	*Ax* *(mm)*	*By* *(nm)*	*Bx* *(mm)*
[0/90]	158	0.16	246	0.39
[0/0/90]	25	0.16	146	0.35
[0/0/0/90]	3	0.13	113	0.29
[0/0/0/0/90]	0	0	99	0.30

Table IV. Surface Parameter Values for Laminates with d = 4t and loading = 1000 MPa.

LAMINATE	*Ay (nm)*	*Ax (mm)*	*By (nm)*	*Bx (mm)*
[0/0/0/90]	3	0.13	113	0.29
[0/0/90/90]	325	0.34	493	0.71
[0/90/90/90]	2974	0.42	1916	1.07

Table V. Surface Parameter Values for different Ply Orientations where d = 4t, a=t and loading = 1000 MPa

LAMINATE	*Ay (nm)*	*Ax (mm)*	*By (nm)*	*Bx (mm)*
[0/0/0/90]	3	0.13	113	0.29
[90/0/0/90]	8	0.16	172	0.14
[0/90/0/90]	4	0.12	124	0.26

From tables II, III, IV and V, it is evident that the A_y value is decreasing with increase in the value of the depth of the crack tip and a decrease in microcrack length. The B_y value is also decreasing with increase in the value of the crack tip and a decrease in microcrack length. With the exception of the two cases in which the microcrack length is *3t* and *4t*, the *By* values are greater than the *Ay* values. The lateral distances are also decreasing with increase in crack tip depth and a decrease in microcrack length. The *Bx* values are also generally greater in magnitude than the *Ax* values. It can be concluded from the above tables that for laminates which have the microcrack thickness equal to or less than half the thickness of the laminate, the sensitivity of the equipment as well as resolving power of the lens must be greater to capture the displacement profile in region A than the one in region B.

6 Conclusions and Recommendations

The finite element analysis performed in this investigation generated the out-of-plane surface displacement field for a number of loaded cross-ply IM7/977-2 laminates containing microcracks in the 90° inner plies. Surface parameters and laminate parameters were identified to correlate surface patterns to both laminate and crack geometry. Included in the laminates tested were $[0/90]_s$, $[0/90/90]_s$ and $[0/0/90]_s$ laminates. The difference in out-of-plane values for these laminates varied between 246 nanometers to 1087 nanometers for a load of 1000 MPa. In digital holography, the sensitivity is reported to be on the order of 10 nm; therefore this type of system is sensitive enough to gather this range in surface displacement data. The lateral distance to the peak values and far-field values were also obtained. These results provide a guideline for choosing a lens powerful enough to spatially resolve the data.

The results indicate that the loading on the laminate is linearly related to the *Uy* displacement values. The location of the peak and far-field values were found to be independent of loading. For a fixed distance of the crack tip below the surface, an increase in microcrack size results in an increase in the difference in the maximum and minimum values. Also as expected, for a fixed microcrack size, as the tip moves farther below the surface, the difference between the maximum and minimum values is minimized. Finally, the ply lay-up in the region between the crack tip and the surface plays a role in influencing this difference value. As expected, an increase in the number of 90° plies in this region results in an increase in the difference between the minimum

and maximum values. This is due to the increase in Poisson's contraction of the *xy* plane and the decrease in stiffness in the *y*-direction. Results also indicate that the lateral distances to the peak and far-field values are independent of loading. These parameters are directly related to the laminate geometry and depend mostly on the size (thickness) of the microcrack.

The present investigation is limited to transverse loadings of cross-ply laminates containing a single microcrack in the inner 90° plies. Future work could include modeling biaxial loading of the laminates as well as multiple microcracks in different plies. Future work could also be aimed at investigating how the material properties influence the surface displacement data. Finally, this work suggests that an experimental investigation aimed at transversely loading some $[0/90]_s$, $[0/90/90]_s$ and $[0/0/90]_s$ specimens and using a technique such as digital holography to gather surface displacement data is warranted.

References

1) M. C. Larson, M. A. Verges, and W. D. Keat, 1999, "Nondestructive Identification of Three-Dimensional Embedded Cracks in Finite Bodies by Inversion of Surface Displacements", *Journal of Fracture Mechanics*, 63 (5), 611-629.

2) S. Choi and B.V. Sankar, " A Micromechanics Method to Predict the Microcracking of the LH2 Composite Tank at Cryogenic Temperature", Univ of Florida, June 2003.

3) T.L.Anderson, "Fracture Mechanics" , 2nd Edition.

4) M. A. Verges, P.J. Schilling, P.D. Herrington, A.K. Tatiparthi, 2003, "Investigation of Microcrack Growth in $[0/90]_s$ Composite Laminates", ASME International Mechanical Engineering Congress and Exposition.

5) ANSYS help documentation

6) D.B. Miracle, S.L. Donaldson, " Introduction To Composites", Air Force Research Laboratory

7) B.D. Agarwal, L.J. Broutman, 1990, " Analysis and Performance of Fiber Composites"

8) J.A.Nairn, Univ. of Utah, USA "Matrix Microcracking in Composites"

9) D.E. Bray, R.K. Stanley , 1997, "Nondestructive Evaluation – A Tool In Design, Manufacturing And Service"

10) M. A. Verges, "Prediction Of Microcracking", April 2001 – Dec 2001.

11) A.S. Ganpatye,Bongtaek oh, K. Maslov, V. Kinra, D.C. Lagoudas, Texas A & M Univ. , "Mechanical Characterization And Ultrasonic NDE Of Cryogenic Composites"

12) P.J. Schilling, B.P.R. Karedla, A.K. tatiparthi, M.A. Verges, P.D. Herrington, "X-ray Computed Microtomography Of Internal Damage In Fiber Reinforced Composite Laminates"

13) P.D. Herrington, P.J. Schilling, M.A. Verges, P.K. Durgam, " Identification Of Critical Surface Displacement Parameters For Characterization Of Subsurface flaws", ASME International Mechanical Engineering Congress and Exposition, Proceedings of Nov, 2002.

14) Sky scan-1072 Micro Scanner Machine Manual

15) M. Honlet, Honlet Optical Systems, Germany, " Nondestructive Testing Of Complex Composite Materials And Structures Using Optical Techniques"

16) G Cloud, 1995, " Optical Methods Of Engineering Analysis"

17) J. Gryzagoridis, University Of Cape town, RSA, " Fundamentals Of Holographic Interferometry, Electrical Speckle Pattern Interferometry (ESPI) and Shearography"

18) J. Tyson, T. Schmidt, K. Galanulis, "Advanced Photogrammetry for Robust Deformation and Strain Measurement", Proceedings of SEM 2002 Annual Conference, Milwaukee, WI, June 2002

19) < http/www.gci.com >

20) D.L. Flaggs and M.H.Kural, " Experimental Determination Of the In Situ Transverse Lamina Strength In Graphite Epoxy Laminates", Journal Of Material Science, Vol 16, 1982, 103 – 115.

21) K.W. Garrett and J.E. Bailey, "Multiple Transverse Fracture in 90 $\pm$ Cross Ply Laminates Of Glass Fiber Rein Forced Polyester", Journal Of Material Science, Vol 12 , 1977, 157 – 168.

Appendix A

Input file

```
*CREATE, FRACT, MAC
/NOPR
NSEL, ALL
*GET, N,NODE,,NUM,MAX
CMSEL,S,CRACKTIP
ESLN
*GET,ELMAX,ELEM,,NUM,MAX
*DO,IEL,1,ELMAX
        ELMI=IEL
        *IF,ELMI,LE,0,EXIT
        *GET,ELTYPE,ELEM,ELMI,ATTR,TYPE
        *IF,ELTYPE,NE,ARG1,CYCLE
        N3 = NELEM(ELMI, 3)
*IF,NSEL(N3),LE,0,CYCLE
N7 = NELEM (ELMI,7)
*IF,NSEL (N7),LE,0,CYCLE
N1 = NELEM(ELMI,1)
N2 = NELEM(ELMI,2)
N5 = NELEM(ELMI,5)
N6 = NELEM(ELMI,6)

X3 = 0.75*NX(N3)
Y3 = 0.75*NY(N3)
Z3 = 0.75*NZ(N3)
X   = 0.25*NX(N2)+X3    !  QUARTER POINT LOCATION(NODE(R))
Y   = 0.25*NY(N2)+Y3
Z   = 0.25*NZ(N2)+Z3

        N = N + 1                               !  NEXT NODE
        N10 = N
        N, N10,X,Y,Z                !  MIDSIDE NODE LOCATION
X = 0.25*NX (N1) +X3
Y = 0.25*NY (N1) +Y3
Z = 0.25*NZ (N1) +Z3

        N = N + 1
        N12 = N
```

```
        N,N12,X,Y,Z
X7 = 0.75*NX (N7)
Y7 = 0.75*NY (N7)
Z7 = 0.75*NZ (N7)
X  = 0.25*NX (N6) +X7
Y  = 0.25*NY (N6) +Y7
Z  = 0.25*NZ (N6) +Z7
        N = N + 1
        N14 = N
        N,N14,X,Y,Z
X = 0.25*NX (N5) +X7
Y = 0.25*NY (N5) +Y7
Z = 0.25*NZ (N5) +Z7
        N = N + 1
        N16 = N
        N, N16, X, Y, Z
        N4 = N3
        N8 = N7
        NSEL, ALL
        TYPE, 3
EN, ELMI, N1, N2, N3, N4, N5, N6, N7, N8          ! REDEFINE THE ELEMENT
EMORE, 0, N10, 0, N12, 0, N14, 0, N16
EMORE,
*ENDDO
CMSEL, U, CRACKTIP                                ! UNSELECT THE TIP NODES
NUMMRG, NODE                                      ! MERGE MIDSIDE NODES
NSEL, ALL                                         ! SELECT ALL EELMENTS
ESEL, ALL                                         ! SELECT ALL EELMENTS
/GOPR
*END


/PREP7
*AFUN, DEG

ET, 1, 45
ET, 2, 45
ET, 3, 95

!!! MATERIAL PROPERTIES

MP, EX, 2, 159E3
MP, EY, 2, 9.43E3
MP, EZ, 2, 9.43E3

MP, PRXY, 2, 0.253
```

```
MP, PRYZ, 2, 0.456
MP, PRXZ, 2, 0.253

MP, GXY, 2, 4.34E3
MP, GYZ, 2, 2.57E3
MP, GXZ, 2, 4.34E3


MP, EZ, 1, 159E3
MP, EY, 1, 9.43E3
MP, EX, 1, 9.43E3

MP, NUXY, 1, 0.456
MP, NUYZ, 1, 0.253
MP, NUXZ, 1, 0.253

MP, GXY, 1, 2.57E3
MP, GYZ, 1, 4.34E3
MP, GXZ, 1, 4.34E3

CSYS, 1
N, 1, 0, 0
NGEN, 14, 50, 1
N, 6, 0.127, 0

CSYS, 0
FILL, 1, 6, 4, 2, 1

N, 606, 0, -0.127, 0
N, 306,0.127,-0.127,0

FILL, 6, 306, 2, 106, 100
FILL, 306, 606, 2, 406, 100
FILL, 601, 606, 4, 602, 1

CSYS, 1
FILL, 5, 605, 5, 105, 100
FILL, 4, 604, 5, 104, 100
FILL, 3, 603, 5, 103, 100
FILL, 2, 602, 5, 102, 100

NDELE, 104
NDELE, 204
NDELE, 304
NDELE, 404
NDELE, 504
```

```
CSYS, 0
N, 104, 0.76200E-01, -0.022, 0
N, 204, 0.075, -0.044, 0
N, 304, 0.065, -0.062, 0
N, 404, 0.050, -0.072, 0
N, 504, 0.026, -0.76200E-01, 0


*Do, I, 5, 505, 100
X = (NX(I+99) +NX(I+101))/2
Y = (NY(I+99) +NY(I+101))/2
N, I+100, X, Y
*ENDDO

CSYS, 0
N, 100, 12.7, 0
N, 200, 12.7, -0.127/3
N, 300, 12.7, -2*0.127/3
N, 400, 12.7, -0.127

FILL, 6, 100, , 7 , 1 , , ,10
FILL, 106, 200, ,107 , 1 , , ,10
FILL, 206, 300, ,207, 1 , , , 10
FILL, 306, 400, ,307, 1 , , , 10

NGEN, 21, 5000, ALL, , , , ,0.25
MAT, 1
TYPE, 1

E, 2, 102, 1, 1, 5002, 5102, 5001, 5001
EGEN, 6, 100, -1

TYPE, 2
EMODIF, 1              !  MODIFY ELEMENTS 1 TO 8 FROM TYPE, 1 TO TYPE2
*REPEAT, 6, 1
NUMMRG, NODE                          !  MERGE COINCIDENT NODES

TYPE, 1
E, 2, 3, 103, 102, 5002, 5003, 5103, 5102
EGEN, 6, 100, -1

E, 3, 4, 104, 103, 5003, 5004, 5104, 5103
EGEN, 6, 100,-1

E, 4, 5, 105, 104, 5004, 5005, 5105, 5104
```

```
EGEN, 6, 100,-1

E, 5, 6, 106, 105, 5005, 5006, 5106, 5105
EGEN, 6, 100,-1

E, 6, 7, 107, 106, 5006, 5007, 5107, 5106
EGEN, 94, 1,-1

E, 106, 107, 207, 206, 5106, 5107, 5207, 5206
EGEN, 94, 1,-1
E, 206, 207, 307, 306, 5206, 5207, 5307, 5306
EGEN, 94, 1,-1

NSEL,ALL
NSYM, Y, 1000, ALL

ESEL,ALL
EGEN, 2, 1000, ALL,  ,  , 1

EGEN, 20, 5000, ALL

NSEL, S, LOC, X, 0
NSEL, R, LOC, Y, 0
CM, CRACKTIP, NODE
/ NERR, 0          ! TEMPORARILY NO WARNINGS OR ERRORS PRINTTOUT
                   ! IN ORDERTO AVOID WARNING MESSAGES DUE TO
                   !MIDSIDE NODES LOCATION

FRACT, 2                    ! CONVERSION MACRO, TYPE 2 SOLID45
                            ! ELEMENTS AROUND CRACK TIP

/NERR, DEFA
NUMMRG, NODE

NSEL,S,LOC,Y,0,0.127
ESLN,S,1,ALL
ESEL,R,MAT,,1
MAT,2
EMODIF,ALL

NSEL,ALL
ESLN,S,,ALL
EPLOT

/SOLUTION
```

```
NSEL, S, LOC, X, 0
D, ALL, UX

NSEL, S, LOC, X, 0
NSEL, R, LOC, Y, -0.127, -0.001
DDELE, ALL, UX

NSEL, S, LOC, Z, 2.5
D,ALL,UZ

NSEL, S, LOC, Y, -0.127
D, ALL, UY

NSEL, S, LOC, X, 12.7
SF,ALL,PRES,-1000

ALLSEL
SOLVE
SAVE

/POST1
NSEL,S,LOC,X,-1,1
NSEL,R,LOC,Z,2.5
ESLN,S,,ALL
PLNSOL,U,Y

/EOF
```

VITA

BalaKishore V Rayasam completed his Bachelors in Mechanical Engineering from Nagarjuna University, India in 2000. He started his masters degree in mechanical engineering at University of New Orleans in June of 2001. Presently he is pursuing his masters from University of New Orleans.